J. Fluid Mech. (2008), *vol.* 607, *pp.* 51–80.
doi:10.1017/S0022112008001808 Printed in the United Kingdom

Flow structure behind two staggered circular cylinders. Part 1. Downstream evolution and classification

J. C. HU AND Y. ZHOU†

Department of Mechanical Engineering, The Hong Kong Polytechnic University, Hung Hom, Kowloon, Hong Kong, China

(Received 13 March 2007 and in revised form 7 March 2008)

Flow structures, Strouhal numbers and their downstream evolutions in the wake of two-staggered circular cylinders are investigated at $Re = 7000$ using hot-wire, flow-visualization and particle-image velocimetry techniques. The cylinder centre-to-centre pitch, P, ranges from $1.2d$ to $4.0d$ (d is the cylinder diameter) and the angle (α) between the incident flow and the line through the cylinder centres is $0^\circ \sim 90^\circ$. Four distinct flow structures are identified at $x/d \geqslant 10$ (x is the downstream distance from the mid-point between the cylinders), i.e. two single-street modes (S-I and S-II) and two twin-street modes (T-I and T-II), based on Strouhal numbers, flow topology and their downstream evolution. Mode S-I is further divided into two different types, i.e. S-Ia and S-Ib, in view of their distinct vortex strengths. Mode S-Ia occurs at $P/d \leqslant 1.2$. The pair of cylinders behaves like one single body, and shear layers separated from the free-stream sides of the cylinders roll up, forming one street of alternately arranged vortices. The street is comparable to that behind an isolated cylinder in terms of the topology and strength of vortices. Mode S-Ib occurs at $\alpha \leqslant 10^\circ$ and $P/d > 1.5$. Shear layers separated from the upstream cylinder reattach on or roll up to form vortices before reaching the downstream cylinder, resulting in postponed flow separation from the downstream cylinder. A single vortex street thus formed is characterized by significantly weakened vortices, compared with Mode S-Ia. Mode S-II is identified at $P/d = 1.2 \sim 2.5$ and $\alpha > 20^\circ$ or $1.5 \leqslant P/d \leqslant 4.0$ and $10^\circ < \alpha \leqslant 20^\circ$, where both cylinders generate vortices, with vortex shedding from the upstream cylinder at a much higher frequency than from the downstream, producing two streets of different widths and vortex strengths at $x/d \leqslant 5.0$. The two streets interact vigorously, resulting in a single street of the lower-frequency vortices at $x/d \geqslant 10$. The vortices generated by the downstream cylinder are significantly stronger than those, originating from the upstream cylinder, in the other row. Mode T-I occurs at $P/d \geqslant 2.5$ and $\alpha = 20^\circ \sim 88^\circ$; the two cylinders produce two streets of different vortex strengths and frequencies, both persisting beyond $x/d = 10$. At $P/d \geqslant 2.5$ and $\alpha \geqslant 88^\circ$, the two cylinders generate two coupled streets, mostly anti-phased, of the same vortex strength and frequency ($St \approx 0.21$), which is referred to as Mode T-II. The connection of the four modes with their distinct initial conditions, i.e. interactions between shear layers around the two cylinders, is discussed.

† Author to whom correspondence should be addressed: mmyzhou@polyu.edu.hk

1. Introduction

Because of its fundamental importance and engineering significance, flow behind two circular cylinders has been investigated extensively. Most previous investigations focused on the wake of two side-by-side or inline cylinders because of their relative simplicity. As a result, our knowledge has been greatly improved on the two types of flow in terms of the dependence on the cylinder centre-to-centre spacing, P/d (d is the cylinder diameter), of the flow structure (e.g. Williamson 1985; Kolář, Lyn & Rodi 1997; Sumner *et al.* 1999; Zhou *et al.* 2001, 2002; Zhou & Yiu 2006), Strouhal number St (e.g. Igarashi 1981, 1984; Kim & Durbin 1988; Xu & Zhou 2004) and forces on the cylinders (e.g. Zdravkovich 1977, 1985, 1987; Mahir & Rockwell 1996). In practice, flow around two staggered cylinders is more important than that around side-by-side or inline arranged cylinders because of its more common occurrence in engineering. This flow is apparently more complicated, depending on the angle of incidence (α) between incident flow and the line through the cylinder centres, as well as P/d, Reynolds number (Re), etc. Some previous investigations are summarized in table 1. These investigations have greatly advanced our knowledge of this flow, in particular, in terms of the time-averaged pressure (C_p), lift (C_L) and drag (C_d) coefficients on the cylinders.

There have been attempts to classify flow around two staggered circular cylinders, mostly based on measured C_L, C_d, St, and C_p, probably motivated by engineering problems such as flow-induced vibrations and aerodynamic noise. Zdravkovich (1977) classified the flow for $P/d = 1.2 \sim 3.0$ and $\alpha = 0^\circ \sim 180^\circ$ with an interval of 30°($Re = 8000$). Depending on whether C_d was greater or less than that in a single-cylinder wake, and whether C_L is positive, negative, or negligible, three regions were identified for both cylinders, i.e. negligible C_L with small C_d, small C_L with small C_d, and repulsive C_L with large C_d. Two more regions were identified for the downstream cylinder, i.e. negligible C_L with large and small C_d, respectively. Sumner *et al.* (2005) investigated C_L, C_d and St in the wake of two staggered circular cylinders at $Re = 3.2 \sim 7.4 \times 10^4$ with $P/d = 1.125 \sim 4.0$ and $\alpha = 0^\circ \sim 90^\circ$. The flow was classified as three types in terms of the pitch ratio: (i) closely spaced ($P/d < 1.5$); (ii) moderately spaced ($1.5 \leqslant P/d \leqslant 2.5$); and (iii) widely spaced ($P/d > 2.5$). Case (i) was characterized by a significant variation in C_L and C_d on both cylinders with α. In case (ii) C_L and C_d changed slightly for the upstream cylinder, but displayed a relatively complicated behaviour for the downstream. In case (iii), C_L and C_d on the upstream cylinder exhibited a negligible variation, and approached their counterparts on an isolated cylinder. Meanwhile, C_d on the downstream cylinder achieved a minimum at $\alpha = 0$. These classifications are useful for engineering design, though providing little information on the flow structure around the cylinders. Another classification is based on vortex shedding frequencies, f_s, in the wake. Kiya *et al.* (1980) measured f_s for $P/d = 1.0 \sim 5.5$, $\alpha = 0^\circ \sim 180^\circ$ with an interval of 15°($Re = 1.58 \times 10^4$), and classified the flow into five regions, depending on whether St was greater or smaller than that in an isolated cylinder wake, and whether vortex shedding from the upstream cylinder occurred. The five regions are characterized by bistable vortex shedding, weak (or no) vortex shedding, St larger and smaller than that in an isolated cylinder wake, and single-body-like vortex shedding, respectively. A classification based on C_L on the downstream cylinder was also proposed. Two regimes were suggested (Zdravkovich 1987): (i) positive C_L (outward-directed) at the cylinder transverse (T/d) and longitudinal (L/d) spacings larger than 2.8 and 0.4, respectively; (ii) negative C_L (inward-directed) at $1.1 < L/d < 3.5$ and $T/d = 0.2$. The former arises

Reference	Reynolds number	Geometrical arrangement	Aspect ratio	Blockage ratio	Turbulent Intensity	Measurements conducted					
						C_d	C_L	C_p	St	VF	Flow structure
Suzuki *et al.* (1971)	1.3×10^3	$P/d = 2.0$, αg 0°–15°	–	–	–	–	–	–	–	–	FV
Suzuki *et al.* (1971)	$1.0–6.3 \times 10^5$	$P/d = 1.1–3.9$, αg 0°–15°	6–18	12–24%	–	√	√	√	–	–	–
Ishigai *et al.* (1972, 1973)	$1.5–15 \times 10^3$	$L/d = 0.68–4.0$, $T/d = 0.5–3.0$	11	9%	–	–	–	√	√	–	FV
Price (1976)	$1.7–8 \times 10^4$	$L/d = 6.0–18.0$, $T/d = 0–2.42$	37, 42	5–12%	1–11%	√	√	√	–	–	FV
Zdravkovich & Pridden (1977)	6×10^4	$L/d = 0–5.0$, $T/d = 0–3.0$	33	5%	0.10%	√	√	√	–	–	–
Kiya *et al.* (1980)	1.58×10^4	$P/d = 0–5.5$, αg 0°–180°	21	2%	0.80%	–	–	–	√	–	–
Price & Païdoussis (1984)	$1.7–7.3 \times 10^4$	$L/d = 1.5–5.0$, $T/d = 0.75–2.0$	24	6%	0.50%	√	√	–	–	–	–
Sun *et al.* (1992)	$3.2–6.5 \times 10^4$	$P/d = 2.2$, αg 12.5°	15	4.9%	0.12%	–	–	√	–	–	–
Gu *et al.* (1993)	6.5×10^5	$P/d = 1.05–2.2$, αg 12.5°	15	5.7%	0.12–10%	√	√	√	–	–	–
Gu & Sun (1999)	5.6×10^3	$P/d = 1.5–2.0$, αg 5°–45°	–	–	–	–	–	–	–	–	FV
Gu & Sun (1999)	$2.2–3.3 \times 10^5$	$P/d = 1.1–3.5$, αg 0°–90°	64	8%	0.20%	√	√	√	√	√	–
Sumner *et al.* (2000)	$0.85–1.35 \times 10^3$	$P/d = 1.0–5.0$, αg 0°–90°	16	13.0%	0.50%	–	–	–	√	–	FV
Sumner *et al.* (2000)	1.9×10^3	$P/d = 1.0–4.0$, αg 0°–90°	27	7.0%	–	–	–	–	–	√	PIV
Sumner & Richards (2003)	$3.2–7 \times 10^4$	$P/d = 2.0–2.5$, αg 0°–90°	24	5.6%	0.60%	–	–	–	√	–	–
Akbari & Price (2005)	8×10^2	$P/d = 1.0–4.0$, αg 5°–70°	–	–	–	–	–	–	√	–	Simulation
Alam & Sakamoto (2005)	5.5×10^4	$P/d = 1.1–6.0$, αg 10°–75°	6	4%	0.50%	–	–	–	√	–	–
Sumner *et al.* (2005)	$3.2–7.4 \times 10^4$	$P/d = 1.125–4.0$, αg 0°–90°	18–24	5.6%	0.60%	√	√	–	√	–	–
Present study	$0.3–7 \times 10^3$	$P/d = 1.2–4.0$, αg 0°–90°	30, 48	3.3–4.2%	0.4–1.2%	–	–	–	–	√	FV, PIV
Present study	7×10^3	$P/d = 1.2–4.0$, αg 0°–90°	48	4.2%	0.40%	–	–	–	√	√	Hot wire

TABLE 1. A summary of previous investigations of two staggered circular cylinders in crossflow. VF, velocity field; FV, flow visualization; PIV, particle image velocimetry.

from the displacement of the fully formed upstream-cylinder wake by the downstream cylinder, and the latter results from the gap flow between the cylinders, which induces a significant inward-directed lift on the downstream cylinder. This classification highlights the role the gap flow plays, and the two different origins of lift forces on the downstream cylinder. However, this classification provides no information on the flow structure around the two cylinders. Gu & Sun (1999) proposed a classification based on measured C_p. They identified three different pressure patterns on the downstream cylinder at $P/d = 1.5$, 1.7 and 2.0, and $\alpha = 0^\circ \sim 90^\circ (Re = 2.2 \sim 4.5 \times 10^5)$. Pattern IB occurred when the downstream cylinder was largely submerged in the wake of the upstream. Pattern IIB was identified when the downstream cylinder, not immersed in the wake of the upstream, displaced the wake and squeezed streamlines into the gap region. Pattern IIIB was observed when the inner shear layer separated from the upstream cylinder no longer reattached on the downstream, and vortex shedding occurred from both cylinders. The three patterns were attributed to shear-layer interference, wake interference and neighbourhood interference, respectively. This classification reflects the connection of C_p on the downstream cylinder with the upstream-cylinder wake, but not the complicated interactions between vortices generated by the two cylinders and their downstream evolution. Sumner *et al.* (2000) classified the flow based on flow patterns around the two cylinders. They performed flow-visualization and particle image velocimetry (PIV) measurements over $P/d = 1.0 \sim 5.0$, $\alpha = 0^\circ \sim 90^\circ$ ($Re = 850 \sim 1900$) and identified nine distinct flow patterns, which were further grouped into single bluff-body flow patterns, flow patterns at small α and those at large α. This classification is valid for $x/d < 6$, where x is the distance from the mid-point between the cylinders. Since the flow behind two staggered cylinders evolves rapidly downstream, one question naturally arises: how should the flow be classified beyond $x/d = 6$?

Numerous investigations have been made previously on St (table 1). Kiya *et al.* (1980) was perhaps the first to report two different St behind two staggered cylinders at large P and α, with the one generated by the upstream cylinder higher than that by the downstream. However, their map of St was incomplete, with the higher St missing in some cases (Alam & Sakamoto 2005). Sumner *et al.* (2000) investigated St over $P/d = 1.0 \sim 5.0$, $\alpha = 0^\circ \sim 90^\circ$ and $Re = 850 \sim 1350$ based on counting vortices when playing back the video tapes of flow visualization, and noted that the inner shear-layer separation from the downstream cylinder was frequently synchronized with alternate shedding from the upstream cylinder. Consequently, the two shear layers might separate from the downstream cylinder at different frequencies. However, Akbari & Price's (2005) numerical data in the two-staggered-cylinder wake showed that the frequency of shear-layer separation from one side of the downstream cylinder was the same as from the other. Sumner *et al.* (2005) measured St extensively using hot wires at $3d$ behind each of two staggered cylinders. Other investigations (e.g. Ishigai *et al.* 1972; Sun *et al.* 1992; Sumner & Richards 2003; Alam & Sakamoto 2005) were conducted over a limited range of P/d and α. Because of the complexity of the two-staggered-cylinder wake compared with a single-cylinder wake, St varies significantly across the wake and evolves rapidly downstream (Ishigai *et al.* 1972; Sumner *et al.* 2000; Zhang & Zhou 2001; Wang & Zhou 2005). This information is still incomplete in the literature and is not systematically documented.

This work aims to provide a classification, based on hot-wire, laser-induced fluorescence (LIF) flow visualization and particle-image velocimetry (PIV) measurements, for the flow structures in a two-staggered-cylinder wake and to investigate systematically the dependence of St on P/d, α and x/d. Experimental

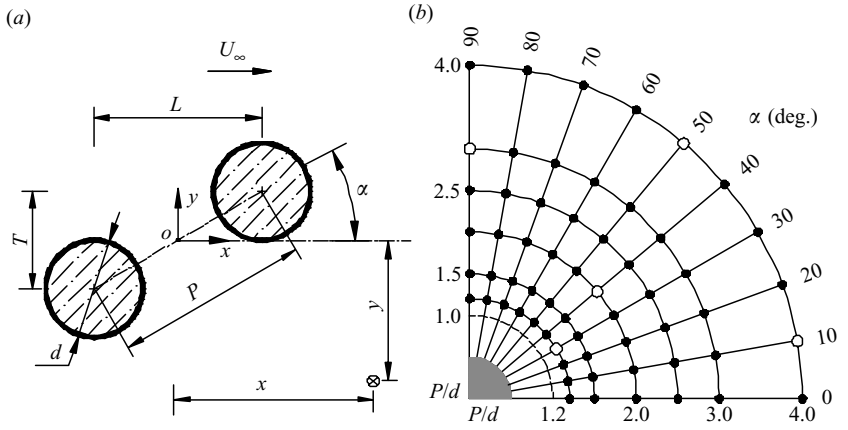

FIGURE 1. (*a*) Experimental arrangement. $x/d = 2.5$, 5, 7.5, 10, 15, 20; $y/d = -3$, -2, -1, 0, 1, 2, 3. ⊗, hot wire. (*b*) Configurations investigated. ●, hot-wire measurement; ○, PIV, hot-wire and flow-visualization measurements.

details are provided in § 2. Strouhal numbers are presented in § 3. Typical flow structures and *St* are given in § 4. The connection of the flow structures with initial conditions is discussed in § 5, and conclusions are given in § 6.

2. Experimental details

Measurements were conducted in a closed-circuit wind tunnel with a 2.4 m long square working section (0.6 m × 0.6 m). The flow in the working section is uniform to within 0.5% and the streamwise turbulence intensity is less than 0.4%. More details of the tunnel are given in Huang, Zhou & Zhou (2006). Figure 1(*a*) presents the experimental arrangement, along with the definitions of P, α, L and T. Coordinates x and y are along the free-stream and lateral directions, respectively, with the origin defined at the mid-point between the cylinder centres. The turbulent wake was generated by two staggered brass circular cylinders of $d = 12.5$ mm. Mounted symmetrically with respect to the mid-plane, the horizontal cylinders spanned the full width of the working section, resulting in a maximum blockage of about 4.2% and an aspect ratio of 48. The angle α ranged from 0° to 90° at an interval of 10° (figure 1*b*). Measurements were also conducted at $\alpha = 84°$, 86° and 88° for $P/d \geqslant 2.5$ (not shown in figure 1*b*) in order to clarify the dependence on α of the difference between the frequencies of vortex shedding from the two cylinders. In view of previous reports (Zdravkovich 1985; Sumner *et al.* 2000) that interference between the cylinders is negligibly small at $P/d > 4.0$, P/d investigated was 1.2, 1.5, 2.0, 2.5, 3.0 and 4.0.

2.1. *Hot-wire measurement*

A Wollaston wire (Pt-10% Rh) of 5 μm in diameter, with a 1 mm long sensing element, was operated in a constant temperature circuit at an overheat ratio of 1.5 and used to measure *St* at $x/d = 2.5$, 5.0, 7.5, 10, 15 and 20. At each station, the wire was traversed across the wake from $y/d = -3$ to 3 with an interval of d. The hot-wire signal (u) was low-pass filtered, offset and amplified, and digitized using a 16 channel (12 bit) A/D board at a sampling frequency of 3 kHz. The sampling duration was 20 s. No calibration was performed. Measurements were conducted at a free-stream velocity $U_\infty = 8.4\ \mathrm{m\,s^{-1}}$, corresponding to $Re\ (\equiv U_\infty d/\nu) = 7000$, where ν was the kinematic viscosity of the air. U_∞ was constantly monitored using a Pitot-static tube connected

to a Furness micro-manometer, its measurement uncertainty being within $\pm 1.0\%$. The power spectral density function, E_u, of u was calculated using a fast Fourier transform. The frequency resolution in E_u was about 0.854 Hz, giving rise to a maximum error of about $\pm 1.0\%$ in the estimate of St ($\equiv f_s d/U_\infty$). The St behind an isolated cylinder was also measured to set a benchmark for comparison.

2.2. *PIV measurement*

A Dantec PIV2100 system was employed to characterize the flow structure behind the cylinders at $Re = 7000$. Five typical configurations were examined, i.e. $P/d = 1.2$ ($\alpha = 30°$), 2.0 (40°), 4.0 (10°), 4.0 (50°) and 3.0 (90°), as indicated by the open circle symbol in figure 1(*b*). One CCD camera (HiSense MkII, gain × 4, double frames, 1344 × 1024 pixels) was used to capture particle images. The flow field was illuminated in the mid-span of the working section by two identical New Wave standard pulsed laser sources with a wavelength of 532 nm and a maximum energy output of 120 mJ. Each laser pulse lasted for 10 ns. A Dantec FlowMap Processor was used to synchronize image acquisition and illumination.

Flow was seeded by smoke, generated from paraffin oil, whose particle size was around 1 μm in diameter. Each digital image covered a flow field of about 148 mm × 112 mm in the (x, y)-plane, about 11.8d and 9.0d in the x- and y-directions, respectively. The image magnification was about 0.11 mm pixel^{-1}. The time interval between two sequential images was 50 μs. Therefore, a particle would travel about 0.42 mm (3.6 pixels or 0.03d) at $U_\infty = 8.4\ \mathrm{m\,s^{-1}}$. An optical filter was used to reduce reflection noise from the cylinder surface, allowing only the green light (generated by the laser source) to pass. About 200 images were taken for each configuration investigated. Data analysis is performed using Dantec's FlowManager. The initial and final particle positions in the flow field, recorded on two consecutive images, are correlated using a statistical spatial cross-correlation algorithm. A detailed mathematical description of the algorithm is given in Raffel, Willert & Kompenhans (1998, § 3.4). The interrogation area is 32 pixels × 32 pixels ($\approx 0.22d \times 0.22d$) with 25% overlap both longitudinally and laterally. More details of the data analysis can be found in Hu, Zhou & Dalton (2006). The in-plane velocity vector field consisted of 54 × 41 vectors (2214 vectors in total), producing the same number of spanwise vorticity components, ω_z. Experimental uncertainties in determining velocities and vorticity are estimated to be 3% and 5%, respectively.

2.3. *Flow visualization*

LIF flow visualization was conducted in a closed-loop water tunnel with a 2.4 m long rectangular test section (width × height = 0.3 m × 0.6 m). See Wang *et al.* (2006) for more details of the tunnel. Two identical acrylic circular tubes with a diameter of 0.01 m were horizontally cantilever-mounted symmetrically with respect to the mid-plane of the working section. The gap between the cylinder end and the tunnel wall was about 0.5 mm. The maximum cylinder blockage was 3.3% and the aspect ratio was 30. The configurations investigated were the same as those of PIV measurements (figure 1*b*). Two pinholes of 0.75 mm in diameter were drilled symmetrically at about 60°, clockwise and anticlockwise, respectively, from the nominal leading stagnation point at the mid-span of each tube. Dye (Rhodamine 6G 99%), whose colour is faint red but becomes metallic green once excited by a laser, was introduced into the flow through the pinholes. A thin laser sheet, which was generated by laser beam sweeping, vertically illuminated the flow field at the mid-plane of the working section. The laser beam was produced by a Spectra-Physics Stabilite 2017 argon ion laser source with a maximum power output of 4 W. A digital video camera recorder (Sony

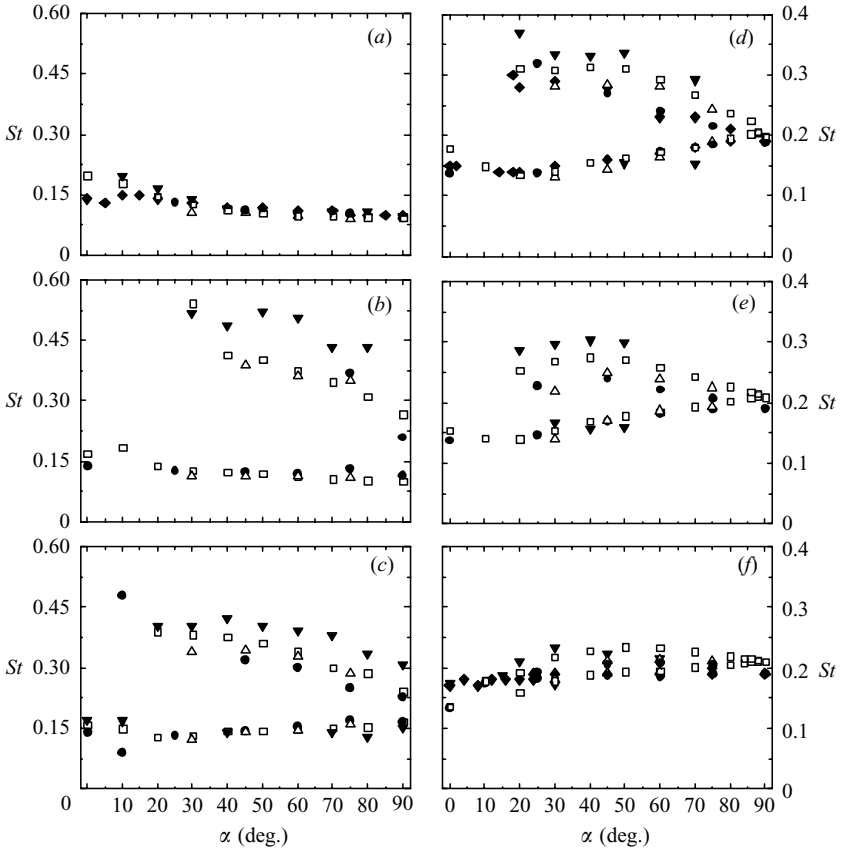

FIGURE 2. Strouhal numbers measured at $x^* = 2.5$ and $Re = 7000$: (*a*) $P^* = 1.2$; (*b*) 1.5; (*c*) 2.0; (*d*) 2.5; (*e*) 3.0; (*f*) 4.0. The data of △, Kiya *et al.* (1980) at $Re = 15\,800$; ▼, Sumner *et al.* (2000) at $Re = 1350$; ●, Alam & Sakamoto (2005) at $Re = 55\,000$; ◆ Sumner *et al.* (2005) at $Re = 50\,000$ are included for comparison. □, present data.

DCR-PC100E) was deployed to record the flow field at a framing rate of 25 frames per second. Flow visualization was conducted at $Re = 300$.

3. Strouhal numbers

The Strouhal number is identified with the frequency at which a pronounced peak occurs in E_u (not shown). Figure 2 presents the dependence of St on α at various P^* measured at $x^* = 2.5$. In this paper, an asterisk denotes normalization by U_∞ and/or d. In general, the present data agree reasonably well, both qualitatively and quantitatively, with measurements by Kiya *et al.* (1980) at $Re = 15\,800$, Sumner *et al.* (2000) at $Re = 1350$, Alam & Sakamoto (2005) at $Re = 55\,000$, and Sumner *et al.* (2005) at $Re = 50\,000$, which are included in the figure. There is some scattering among the data, probably arising from different experimental conditions, such as Re, turbulent intensity, cylinder aspect ratio and blockage. The agreement provides a validation for the present measurement. For $P^* = 2.5$–4.0 and $\alpha = 70°$– $88°$, two different St were presently detected. In contrast, Sumner *et al.* (2000) observed only one St for the same P^* and α. The discrepancy probably results from different techniques to estimate f_s. Sumner *et al.* (2000) estimated vortex shedding frequencies

by counting and timing individual vortices on a frame-by-frame basis from flow-visualization data. Their approach may suffer from a relatively high measurement uncertainty, about 5%, because of the insufficient number of vortices recorded on the video and the modulations of the original vortex frequencies and flow structure under the interactions of shear layers, which make it difficult to count accurately.

At $P^* \leqslant 1.2$ (figure 2*a*), only one *St* is detected, regardless of α, implying the occurrence of one single vortex street. At such a small spacing, the two cylinders behave like one body (Kiya *et al.* 1980; Sumner *et al.* 2000) and shear-layer separation occurs only from the free-stream sides of the cylinder pair, resulting in one frequency of vortex shedding (see figure 4 of Sumner *et al.* 2000). *St* progressively decreases from about 0.2 to 0.09 as α varies from 0° to 90°. This is reasonable, for the increasing α leads to an increasing effective width of the 'single-body-like' cylinder pair and hence decreasing *St*. *St* drops faster for $\alpha \leqslant 40°$ and more slowly for $\alpha > 40°$, as observed by Sumner *et al.* (2000).

At $P^* = 1.2$–1.5, the vortex shedding frequency may vary from one to two, depending on α (not shown). At $P^* = 1.5 \sim 4.0$ (figure 2*b*–*f*), two distinct *St* may occur beyond a critical α. This critical α depends on P^*, a larger P^* corresponding to a smaller critical α. The values of *St* higher and lower than that ($St \approx 0.21$) in an isolated cylinder wake are attributed to vortex shedding from the upstream and downstream cylinders, respectively (Zdravkovich 1985; Sumner *et al.* 2000). In the presence of a downstream cylinder, the base pressure behind the upstream cylinder is high, relative to that in a single-cylinder wake, as inferred from the reduced C_d (see figure 20 of Zdravkovich 1977) on the upstream cylinder. Correspondingly, the frequency of vortex shedding from the upstream cylinder exceeds that ($\sim$0.21) in an isolated cylinder wake. This phenomenon is to some extent analogous to the corner effect on a square cylinder (e.g. Hu *et al.* 2006). Once the leading sharp corners are rounded, the base pressure and the vortex shedding frequency increase. While the upstream cylinder is subjected to an incident flow velocity U_∞, the downstream cylinder is submerged in the wake of the upstream cylinder, that is, the incident flow velocity to the downstream cylinder is lower than U_∞, which contributes, along with a higher turbulence level, to the lower *St* (<0.21) associated with the downstream cylinder. The difference between the two *St* tends to diminish with increasing P^* or α owing to weakened cylinder interference. At $P^* \geqslant 2.5$ and $\alpha \geqslant 88°$ (figure 2*d*–*f*), the frequencies of vortex shedding from the two cylinders are almost the same, about 0.21, as in an isolated cylinder wake or the two-coupled-street regime in a two side-by-side cylinder wake (e.g. Bearman & Wadcock 1973; Zhou *et al.* 2002). The maximum difference between them is about 1%.

At $P^* = 1.5$ (figure 2*b*), only one *St*, smaller than 0.21, is observed at $\alpha \leqslant 20°$. At such small P^* and α, the gap flow is not dynamically important and is not evident in flow visualization; as at $P^* \leqslant 1.2$ (figure 2*a*), vortices are shed only from the free-stream sides of the cylinders, thus resulting in one vortex street (see figure 5*a*–*c* of Gu & Sun 1999). Two different vortex frequencies are observed for $\alpha > 20°$, suggesting the occurrence of two vortex streets. At a large α, the gap flow between the cylinders is biased towards the upstream cylinder side, generating one wide street behind the downstream cylinder and one narrow street behind the upstream cylinder (see figure 13*d* of Sumner *et al.* 2000), which are associated with a lower and a higher *St*, respectively. The higher and the lower *St* ranges are $0.27 \sim 0.54$ and $0.10 \sim 0.13$, respectively. The maximum ratio of the higher *St* to the lower is about 4.2, which occurs at $\alpha = 30°$, falling into the range ($4 \sim 5$) observed by Sumner *et al.* (2000). The higher *St* (0.54) is larger than Kiya *et al.*'s (1980) report (0.39)

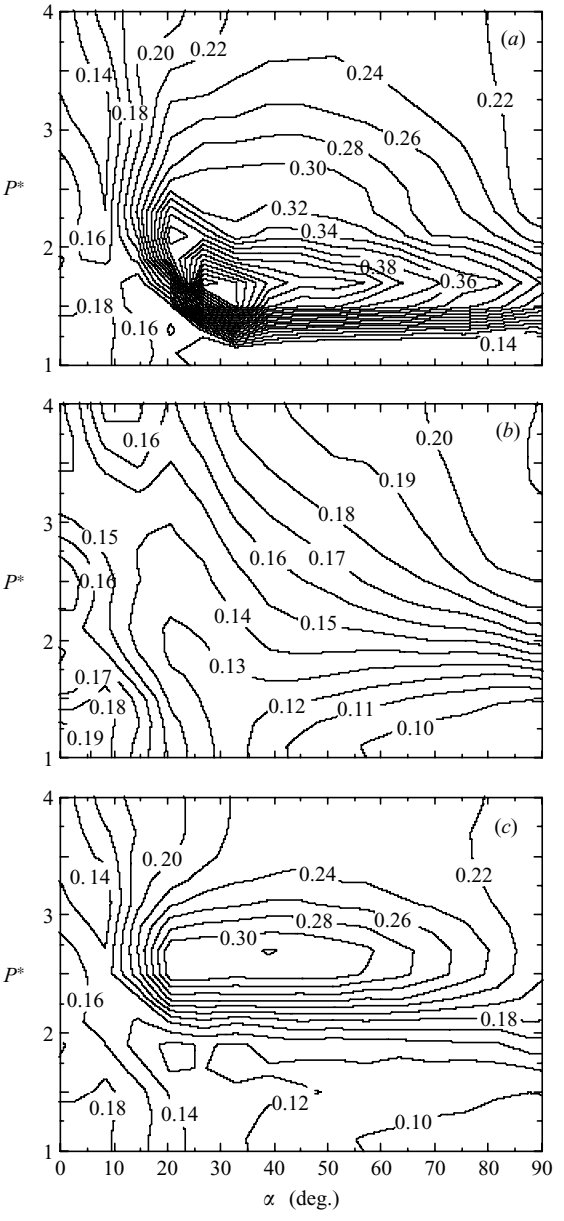

FIGURE 3. Iso-contours of Strouhal number ($Re = 7000$): (*a*) upstream-cylinder-generated vortices, $x^* = 2.5$, cutoff level = 0.14, increment = 0.02; (*b*) downstream-cylinder-generated vortices, 2.5, 0.10, 0.01; (*c*) upstream-cylinder-generated vortices, 10.0, 0.10, 0.02.

but comparable to Sumner *et al.*'s (2000) measurement (0.52). The ratio is 2.7 at $\alpha = 90°$, in agreement with previous reports ($\sim$3.0) for two side-by-side cylinders (e.g. Ishigai *et al.* 1972; Bearman & Wadcock 1973). Similar observations are made at $P^* = 2.0 \sim 4.0$ (figure 2*c–f*) beyond a critical α. Below the critical α ($\leqslant 10°$), only one *St* (<0.21) is identified at $P^* = 2.0 \sim 4.0$ (figure 2*c–f*).

In order to obtain the overall picture of the *St* dependence on P^* and α, the *St* map is presented in figure 3, which is drawn based on measured *St* at $x^* = 2.5$ and 10. The

St map at $x^* = 5$, is almost the same as at $x^* = 2.5$, and is therefore not presented. As is evident in figure 2, St may bifurcate at $x^* = 2.5$, the higher and lower values being ascribed to vortex shedding from the upstream and the downstream cylinders, respectively. As such, figures 3(a) and 3(b) present the St maps at $x^* = 2.5$ associated with the upstream and downstream cylinders, respectively. The iso-contours of St (figure 3a,b) display many similarities to Kiya *et al.*'s (1980) measurement at $x^* \approx 3$. It is worth mentioning that at $P^* = 1.7$ and $\alpha = 90^\circ$, St is 0.30 (figure 3a) and 0.13 (figure 3b) at $x^* = 2.5$, respectively, in good agreement with previous reports in a two-side-by-side cylinder wake (e.g. Bearman & Wadcock 1973; Williamson 1985; Kim & Durbin 1988; Wang & Zhou 2005). Following Zdravkovich (1985), the higher and the lower St at $\alpha = 90^\circ$ (two side-by-side cylinders) are ascribed to the 'upstream' and the 'downstream' cylinders, respectively.

In figure 3(a), St is low at $P^* \leqslant 1.2$, smaller than that (0.21) behind an isolated cylinder, apparently because the two cylinders behave like a single body; it is also low at $\alpha \lesssim 10^\circ$ for the whole range of P^* investigated here. Other than at small P^* or α, St exceeds 0.21, similarly to Kiya *et al.*'s (1980) region 1 (see their figure 9). High St occurs mostly in the region of $P^* = 1.5 \sim 2.5$ and $\alpha = 20^\circ \sim 70^\circ$, where vehement interference between the cylinders leads to a gap flow biased towards the upstream cylinder side, forming a narrow wake of a high St. The highest St, about 0.57, occurs at $P^* = 1.7$ and $\alpha = 26^\circ$. At $P^* \geqslant 3.5$ and $\alpha \geqslant 30^\circ$, interference between the cylinders is weakened and the frequency of vortex shedding from the upstream cylinder approaches that behind an isolated cylinder, i.e. $St \approx 0.22$. Note that at $P^* = 1.2 \sim 1.5$ and $\alpha = 20^\circ \sim 90^\circ$ the contours are densely populated, implying a rapid change in St with a variation in P^* or α. The observation is ascribed to a drastic change in the flow structure. For instance, at $\alpha = 30^\circ$ ($P^* = 1.2$), shear layers around the two cylinders separate from the free-stream sides and roll up to form one single vortex street of $St = 0.128$ (figure 2a). As P^* increases to 1.5, the gap flow may suddenly penetrate into the base region (see figure 13d of Sumner *et al.* 2000), generating a narrow wake of $St = 0.543$ (see figure 2b) behind the upstream cylinder. This rapid change in St is also evident at $P^* = 1.5 \sim 3.5$ and $\alpha = 10^\circ \sim 20^\circ$. For $\alpha \leqslant 10^\circ$, vortex shedding from the downstream cylinder is locked in with that from the upstream and consequently only one St smaller than 0.21 is identified (figure 2e, f), and only one street occurs (see figure 4b of Xu & Zhou 2004). With increasing α, say at $\alpha = 30^\circ$, a gap flow is formed between the cylinders, producing a narrow and a wide wake behind the upstream and the downstream cylinder (see figure 13c of Sumner *et al.* 2000), respectively. Accordingly, the frequency of vortex shedding from the upstream cylinder is significantly higher (figure 2c–f) than that from the downstream or in the isolated cylinder wake. It may be concluded that a rapid change in St associated with the upstream cylinder suggests a change in the wake structure.

The iso-contours of St in figure 3(b) are different from those in figure 3(a). In general, the contour level ranges between 0.1 and 0.21, corresponding to Kiya *et al.*'s (1980) region 2 where St is smaller than that behind an isolated cylinder, and varies rather smoothly, without any rapid change. The lowest St, about 0.1, occurs at $P^* \approx 1.0$ and $\alpha \approx 90^\circ$, which is essentially one body with an effective width of 2d. The highest St is approximately 0.21, occurring at $P^* \approx 1.0$ and $\alpha \approx 0^\circ$ or at $P^* \geqslant 2.5$ and $\alpha \approx 90^\circ$, which agree with previous measurements in a two-tandem-cylinder wake (e.g. Xu & Zhou 2004) and a two-side-by-side cylinder wake (Bearman & Wadcock 1973), respectively. St steadily rises with P^* for $\alpha \geqslant 20^\circ$. The contours are densely populated at $1.2 < P^* \leqslant 2.5$, but are separated more widely at $P^* > 2.5$, indicating a fast and slow rise, respectively. At $\alpha \leqslant 10^\circ$, St declines slowly from 0.2 at $P^* \geqslant 1.0$

to about 0.14 at $P^* \approx 3.2$, and then increases slightly with P^*. This observation resembles the behaviour of St in a two-tandem-cylinder wake (e.g. Ishigai 1981; Xu & Zhou 2004). For instance, Xu & Zhou (2004) reported that St in a two-tandem-cylinder wake decreased from about 0.25 at $P^* = 1.0$ (see their figure 3) to 0.15 at $P^* \approx 4.0 (Re = 7000)$, and then rose slowly with increasing P^*. Apparently, St in a two-staggered-cylinder wake at $\alpha \leqslant 10^\circ$ mimics that in a two-tandem-cylinder wake.

At $x^* = 10$, St again displays two distinct values, depending on P^* and α. The iso-contours of the lower St are identical to those in figure 3(b) and are therefore not shown. This observation suggests that the frequency of vortex shedding from the downstream cylinder remains unchanged and persists at $x^* = 10$ and even farther. However, the iso-contours of the higher St (figure 3c) appear very different from their counterparts at $x^* = 2.5$ (figure 3a), except at $P^* \leqslant 1.2$ or at $\alpha \leqslant 10^\circ$ or at $P^* \geqslant 2.5$ and $\alpha > 20^\circ$. The Strouhal numbers larger than 0.31 disappear from the contours, suggesting vigorous interactions between and dynamic evolution of vortical structures, which will be examined in the following section.

4. Classification of flow structures

The power spectral density function E_u of the signal u is examined across the wake over $x^* = 2.5 \sim 20$ for all the configurations shown in figure 1(b), along with qualitative LIF flow-visualization photographs and quantitative PIV-measured vorticity contours. Four distinct flow structures, depending on P^* and α, are identified, i.e. two single-street modes (S-I and S-II) and two twin-street modes (T-I and T-II). Mode S-I is further divided as two types, i.e. S-Ia and S-Ib, because of a pronounced difference between their vortex strengths. The major characteristics of the flow structures are summarized in table 2 for each mode. The P^* and α ranges for each mode are also given largely based on the flow-visualization, PIV and St data. The resolution of the ranges is limited to the grid size of figure 1(b), i.e. $\Delta P^* = 0.5$ for $P^* = 1.0 \sim 3.0$ and $\Delta P^* = 1.0$ for $P^* = 3.0 \sim 4.0$, and $\alpha = 10^\circ$. The modes are further compared with Sumner *et al.*'s (2000) near-wake flow patterns. While Sumner *et al.*'s flow patterns are identified based on the flow structure at $x^* < 6$, the present classification is made based on the flow structure beyond $x^* = 6$. Five configurations are presented in detail in this section, i.e. $P^* = 1.2$ ($\alpha = 30^\circ$), 2.0 (40°), 4.0 (10°), 4.0 (50°) and 3.0 (90°), representing Modes S-Ia, S-Ib, S-II, T-I and T-II, respectively.

4.1. *Mode S-I*

Mode S-I, including S-Ia and S-Ib, displays an alternately arranged vortex street, which is reasonably antisymmetrical about the centreline, similarly to the Kármán vortex street behind a single cylinder. This mode occurs at small $P^* \leqslant 1.2$ or $\alpha \leqslant 10^\circ$, where only one St (<0.21) is identified at $x^* \geqslant 2.5$. Mode S-Ia occurs when the two staggered cylinders are in close proximity, i.e. $P^* \leqslant 1.2$, irrespective of α, or $P^* \leqslant 1.5$ and $\alpha \leqslant 20^\circ$; its vortex strength is comparable to that in an isolated cylinder wake. On the other hand, Mode S-Ib corresponds to a small angle of incidence ($\alpha \leqslant 10^\circ$) and a greater P^* (>1.5) and its vortex strength is significantly smaller, compared with Mode S-Ia.

4.1.1. *Mode S-Ia*

One typical example of Mode S-Ia is shown in figure 4. The LIF flow-visualization photograph (figure 4a, $Re = 300$) indicates that shear layers separated from the free-stream sides of the cylinder pair roll up to form one alternate vortex street. The

Flow mode	Geometrical arrangement	Correspondence with the patterns of Sumner *et al.* (2000)	Key features	
			Frequency	Flow structure
Single-street				
S-I				
S-Ia	$P^* \leqslant 1.2$, $\alpha = 0° \sim 90°$; $P^* \leqslant 1.5$, $\alpha \leqslant 20°$	SBB1, SBB2, BB, SLR	One pronounced peak in E_u across the wake	Single vortex street at $x^* \geqslant 5$. The vortex strength is comparable to that behind an isolated cylinder
S-Ib	$P^* > 1.5$, $\alpha \leqslant 10°$	SLR, VI	One broadbanded and less pronounced peak in E_u across the wake	Single vortex street at $x^* \geqslant 5$. The vortex strength is significantly weaker than that of Mode S-Ia
S-II	$1.2 < P^* < 2.5$, $\alpha > 20°$; $1.5 \leqslant P^* \leqslant 4.0$, $10° < \alpha \leqslant 20°$	IS, VPE, VPSE	Two different vortex frequencies at $x^* \leqslant 5$, but only the lower frequency discernible at $x^* \geqslant 10$	Single asymmetric vortex street at $x^* \geqslant 10$. Vortices are significantly stronger on the downstream cylinder side than on the upstream cylinder side
Twin-street				
T-I	$P^* \geqslant 2.5$; $20° < \alpha < 88°$	SVS	Two distinct vortex frequencies identified at $x^* = 2.5 \sim 20$	Two streets at $x^* \geqslant 10$. Downstream-cylinder-generated vortices are significantly stronger than upstream-cylinder-generated ones
T-II	$P^* \geqslant 2.5$, $\alpha \geqslant 88°$	SVS	Two streets of the same vortex frequency ($St \approx 0.21$)	Two coupled Kármán vortex streets, mostly symmetrical about the flow centreline

TABLE 2. Typical flow structures, their major characteristics and correspondence with patterns identified by Sumner *et al.* (2000).

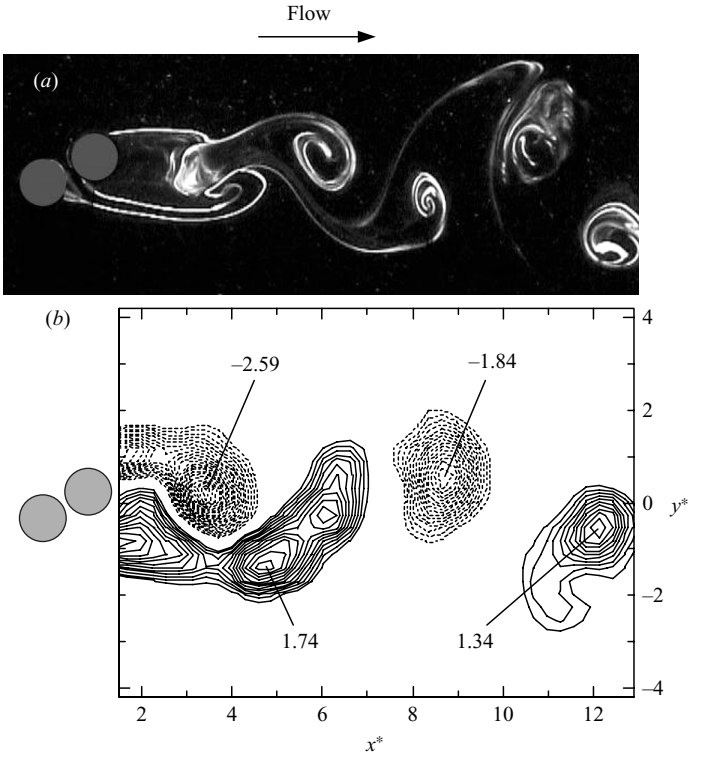

FIGURE 4. Typical instantaneous flow structure of Mode S-Ia ($P^* = 1.2$, $\alpha = 30°$). (*a*) Flow visualization ($Re = 300$); (*b*) PIV-measured vorticity contours ($Re = 7000$), $\omega_z^* = \omega_{zd}/U_\infty$, the cutoff level $= \pm 0.3$, the contour increment $= \pm 0.1$.

gap flow between the cylinders deflects towards the upstream cylinder side and subsequently joins with the outer shear layer separating from the free-stream side of the upstream cylinder to form the vortex of positive sign (in a right-handed coordinate system), whereas the outer shear layer separating from the free-stream side of the downstream cylinder rolls up to form the vortex of negative sign on the other side of the wake, generating one alternately arranged vortex street (figure 4*a*).

The vortex strength of Mode S-Ia is comparable to that in an isolated cylinder wake. Figure 4(*b*) presents the contours of PIV-measured instantaneous vorticity, $\omega_z^* = \omega_z d/U_\infty$. The cutoff level in figure 4*b* and those that follow was set at $|\omega_z^*| = 0.3$, about 10% of the maximum vorticity. The maximum vorticity concentration in figure 4(*b*) is approximately the same as that in a single-cylinder wake; for instance, it is -2.59 at $x^* \approx 3.2$ in figure 4(*b*) and -2.64 at $x^* \approx 3.0$ in figure 4 of Hu *et al.* (2006; $Re = 2600$). The vortex wavelength in figure 4(*b*) appears longer than its counterpart in a single-cylinder wake, apparently because of a lower *St* (figure 2*a*) and approximately the same convection velocity, U_c (comparison is not shown).

E_u (figure 5) displays one pronounced peak at $f^* = 0.128$ across the wake at $x^* = 2.5 \sim 10$. The amplitude of the peaks at various lateral locations is symmetrical about $y^* = 0$. Another minor peak is also discernible at $2f^* = 0.256$. A similar observation was made by Sumner *et al.* (2005). The observation is consistent with the single street of antisymmetrically arranged vortices.

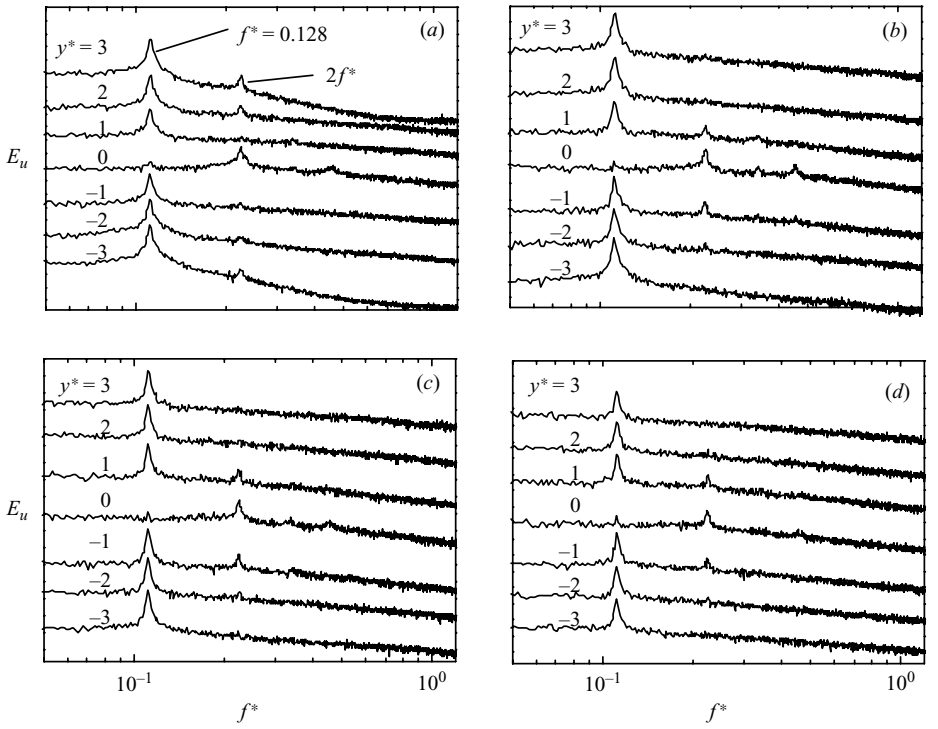

FIGURE 5. Power spectral density function, E_u, of the hot-wire signal u measured at (a) $x^* = 2.5$, (b) 5, (c) 7.5, (d) 10. $P^* = 1.2$, $\alpha = 30^\circ$ (Mode S-Ia). $Re = 7000$.

4.1.2. *Mode S-Ib*

Though approximately antisymmetrically arranged as Mode S-Ia (figure 6*a*), Mode S-Ib is characterized by significantly weaker vortices (figure 6*b*); its maximum vorticity concentration is only about half of that in Mode S-Ia and the vortex size is significantly smaller (see figure 4*b*). The initial conditions of the vortex formation are distinct between Modes S-Ia and S-Ib. In Mode S-Ia, the vortices originate largely from the rollup of shear layers from the free-stream sides of the two cylinders. In Mode S-Ib, the shear layer separated from the upper side of the upstream cylinder reattaches on the downstream cylinder (figure 6*a*). This reattachment may postpone, compared with an isolated cylinder wake, flow separation from the downstream cylinder, resulting in weakened vortices (Zhou & Yiu 2006). Sumner & Richard (2003) measured the forces on the downstream cylinder and observed, at $P^* = 2.0$ or 2.5 ($Re = 3.2 \sim 7.0 \times 10^4$), the maximum inward-directed C_L ($C_L < 0$) and the minimum C_d at $\alpha = 9^\circ$. Similar lift and drag behaviours were reported by Zdravkovich (1977) at $1.1 < L^* < 3.5$, $T^* = 0.2$ ($Re = 6.0 \times 10^4$), i.e. $P^* = 1.1 \sim 3.5$, $\alpha = 5^\circ \sim 16^\circ$. The occurrence of the minimum C_d is consistent with the postponed flow separation in Mode S-Ib. The vortices appear irregular in shape (figure 6*b*), in particular those on the upstream cylinder side ($y^* < 0$), probably owing to interactions between the shear layers separated from the upstream cylinder and the downstream cylinder. These observations are linked to the constant interruption of alternate vortex shedding from the downstream cylinder because of shear-layer reattachment (Sumner *et al.* 2000).

E_u (figure 7) displays only one prominent peak from $x^* = 2.5$ to 10, apparently owing to the predominant vortices. At $\alpha \leqslant 10^\circ$ and $P^* > 1.5$, vortex shedding from

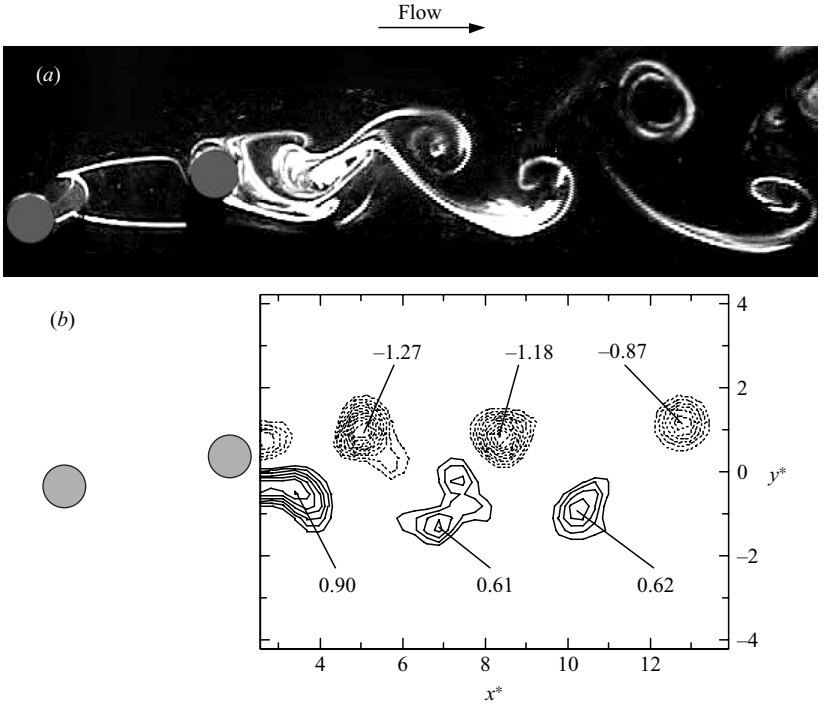

FIGURE 6. Typical instantaneous flow structure of Mode S-Ib ($P^* = 4.0$, $\alpha = 10°$). (*a*) Flow visualization ($Re = 300$); (*b*) PIV-measured vorticity contours ($Re = 7000$), the cutoff level $= \pm 0.3$ and the contour increment $= \pm 0.1$.

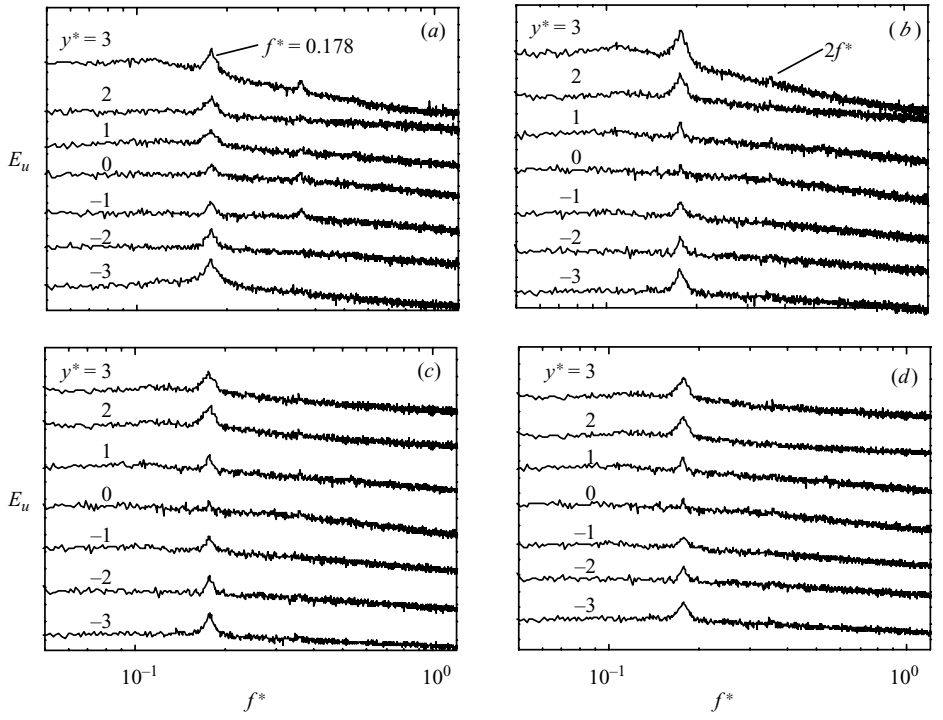

FIGURE 7. Power spectral density function, E_u, of the hot-wire signal u measured at (*a*) $x^* = 2.5$, (*b*) 5, (*c*) 7.5, (*d*) 10. $P^* = 4.0$, $\alpha = 10°$ (Mode S-Ib). $Re = 7000$.

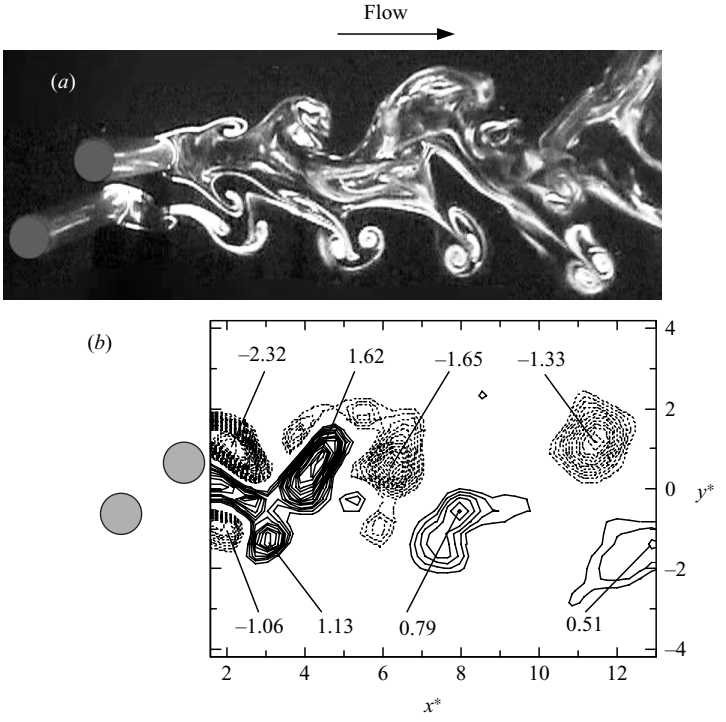

FIGURE 8. Typical instantaneous flow structure of Mode S-II ($P^* = 2.0$, $\alpha = 40°$). (*a*) Flow visualization ($Re = 300$); (*b*) PIV-measured vorticity contours ($Re = 7000$), the cutoff level = ± 0.3, the contour increment = ± 0.1.

the downstream cylinder, probably triggered by the arrival of shear layers or vortices, is locked in with that from the upstream. The peak in E_u is much broader and less pronounced, compared with that in Mode S-Ia (figure 5), internally consistent with the weaker vortices (figure 6*b*). Furthermore, the second harmonic is hardly discernible. The observations imply less quasi-periodic vortex shedding in Mode S-Ib than in Mode S-Ia, consistent with previous reports. Kiya *et al.* (1980) observed weak vortex shedding from two staggered cylinders at $P^* \leqslant 2.5$ and $\alpha < 20°$. See region 2 in their figure 9. Sumner & Richard (2003) reported that, at $P^* = 2.0 \sim 2.5$ and $2° < \alpha < 15°$, the Strouhal number data were unreliable since the peaks in the power spectral density functions of force signals were either absent or broadbanded.

4.2. *Mode S-II*

Mode S-II occurs at $1.2 < P^* < 2.5$ for $\alpha > 20°$ or $1.5 \leqslant P^* \leqslant 4.0$ for $10° < \alpha \leqslant 20°$. Figure 8(*a*) presents one LIF flow-visualization photograph of the typical flow structure. The upstream and the downstream cylinder produce a narrow and a wide street, corresponding to a high and a low vortex frequency, respectively. The two streets interact vigorously. The shear layer separated from the free-stream side of the downstream cylinder forms the vortices of negative sign. The two upstream-cylinder-generated cross-stream vortices in the narrow street appear amalgamating with the downstream-cylinder-generated vortex of positive sign in the lower row of the wide street. Because of the cancellation of positive and negative vorticity during amalgamation, the vortex thus formed is expected to be weaker than the

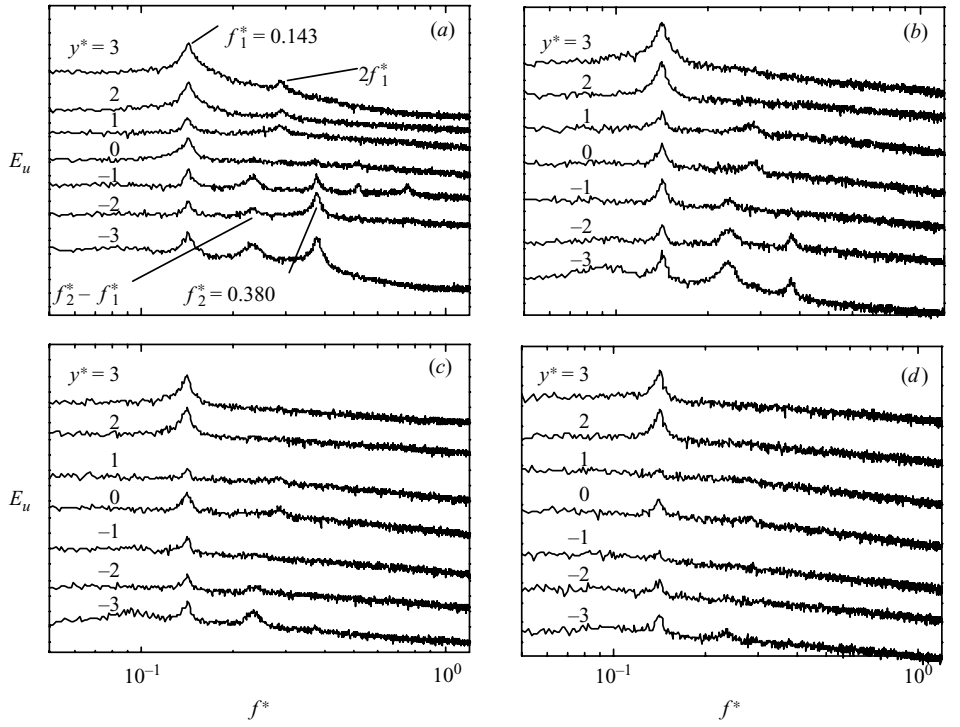

FIGURE 9. Power spectral density function, E_u, of the hot-wire signal u measured at (*a*) $x^* = 2.5$, (*b*) 5, (*c*) 7.5, (*d*) 10. $P^* = 2.0$, $\alpha = 40^\circ$ (Mode S-II). $Re = 7000$.

negative-signed vortex in the wide street. Beyond $x^* > 6$, a single alternate vortex street is seen.

The PIV-measured vorticity contours (figure 8*b*) essentially reconfirm the observation based on LIF flow visualization. At $x^* < 5$, two streets may be identified. The upstream-cylinder-generated vortices are significantly weaker. This is expected since there is a shorter time for the upstream cylinder to accumulate vorticity in view of its much higher vortex shedding frequency. The downstream-cylinder-generated vortices in the lower row are shed with considerably lower strength than those in the upper row. Their amalgamation with the two cross-stream upstream-cylinder-generated vortices in the narrow street forms an even weaker vortex, with its vorticity concentration not exceeding half of that associated with the downstream-cylinder-generated vortices in the upper row. Only one alternate street is identified at $x^* > 6$, which is significantly asymmetric about $y^* = 0$. Vigorous interaction between the two streets at $x^* < 5$ corresponds to a significant increase in C_L on the downstream cylinder. Zdravkovich (1977) suggested that the maximum outward-directed lift force ($C_L > 0$) occurred for $L^* > 2.8$ and $T^* > 0.4$, i.e. $P^* > 2.83$ and $\alpha > 13^\circ$, arising from the displacement of the upstream-cylinder wake by the flow around the downstream cylinder. Gu & Sun (1999) also observed an appreciable C_L at $P^* = 1.7$ and $\alpha = 15^\circ \sim 16^\circ (Re = 2.2 \times 10^5)$.

The downstream evolution of the flow structure is represented well in E_u measured at various stations (figure 9). At $x^* = 2.5$ (figure 9*a*), E_u displays a prominent peak at $St_1 = 0.143$ across the wake, whose second harmonic is also discernible at $y^* > 0$. This peak is apparently due to vortex shedding from the downstream cylinder. At

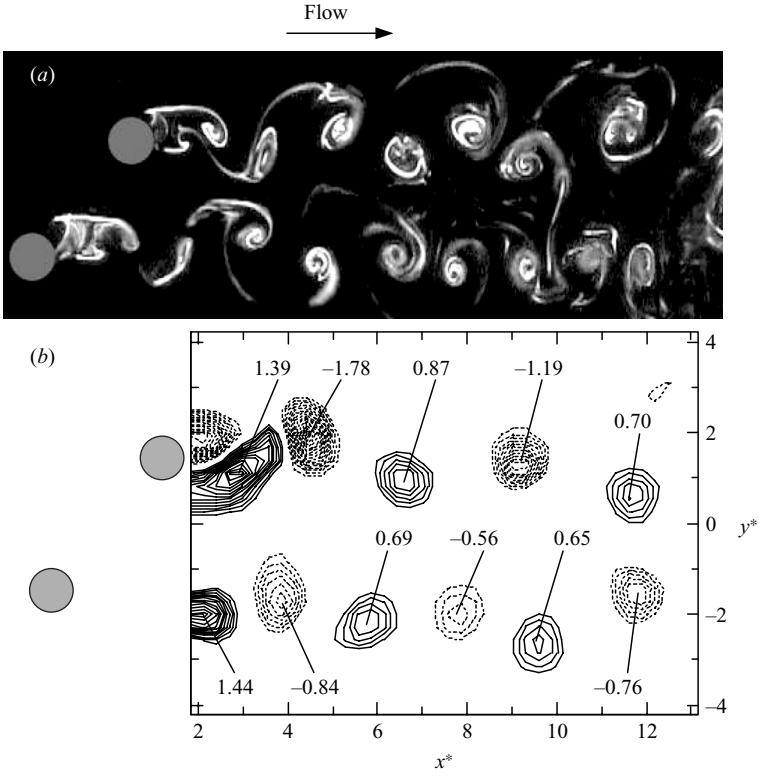

FIGURE 10. Typical instantaneous flow structure of Mode T-I ($P^* = 4.0, \alpha = 50°$): (*a*) Flow visualization ($Re = 300$); (*b*) PIV-measured vorticity contours ($Re = 7000$), the cutoff level = ± 0.3, the contour increment = ± 0.1.

$y^* < 0$, another less pronounced peak is also identifiable in E_u at $St_2 = 0.380$, and is ascribed to vortex shedding from the upstream cylinder. A minor peak may be identified at $St_2 - St_1$ below $y^* = 0$, probably resulting from interactions between the two vortex streets. The three peaks persist in E_u at $x^* = 5$ (figure 9*b*). While the peak at St_1 is growing in magnitude, that at St_2 retreats. Beyond $x^* = 5$, only the peak at St_1 is essentially identified; the one at St_2 has vanished (figure 9*c*, *d*). Furthermore, the peak at St_1 is appreciably stronger at $y^* > 0$ than at $y^* < 0$, reconfirming the observation from LIF flow-visualization and PIV data that the vortex, produced out of the amalgamation of three vortices, in the lower row of the wake ($x^* > 5$) is considerably weaker than that in the upper row, implying an asymmetrical wake. The observation is similar to that reported in the asymmetrical flow regime behind two side-by-side cylinders, e.g. at $P^* = 1.7$ in Wang & Zhou (2005), who suggested that the vortex frequency in the wide wake ($y^* > 0$) is dictated by the shear-layer thickness.

4.3. *Mode T-I*

Mode T-I occurs at $P^* \geqslant 2.5$ and the range of $\alpha = 20° \sim 88°$. The typical flow structure is illustrated in figure 10. Two distinct vortex streets are observed at $x^* = 0 \sim 10$ and even further, in distinct contrast with the two single-street modes, i.e. S-I and S-II. This flow structure occurs when the downstream cylinder is not immersed in the wake of the upstream cylinder, yet the two cylinders are close enough to interfere with each other (Akbari & Price 2005). In figure 10(*a*), the two streets tend to be anti-phased,

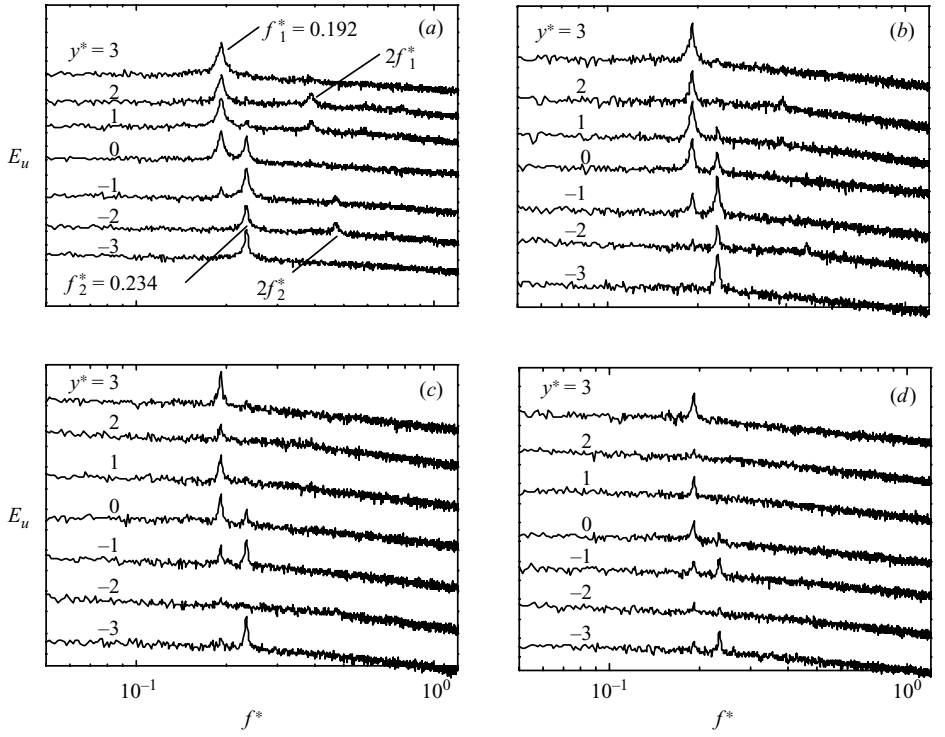

FIGURE 11. Power spectral density function, E_u, of the hot-wire signal u measured at (a) $x^* = 5$, (b) 10, (c) 15, (d) 20. $P^* = 4.0$ and $\alpha = 50^\circ$ (Mode T-I). $Re = 7000$.

with the inner (or outer) vortices occurring at approximately the same phase, in the near wake (up to $x^* \approx 10$). This anti-phase relationship disappears beyond $x^* \approx 10$. The in-phase relationship, though less stable than the anti-phased, was also observed (not shown). On the other hand, the PIV-measured vorticity contours (figure 10b) display neither an anti-phased nor in-phase relationship between the two streets. Similarly to the near wake of Mode S-II, the downstream cylinder generates vortices at a higher frequency than the upstream, as inferred from counting vortices in figure 10(a), though the two frequencies do not differ greatly as in Mode S-II, which will be confirmed later by E_u. This is reasonable since the downstream cylinder always produces vortices at a lower frequency (Zdravkovich 1985), implying a longer time for the shear layers around the cylinder to accumulate vorticity before separation. As a consequence, the downstream-cylinder-generated vortex street is characterized by a higher vortex strength (figure 10b) and an appreciably larger width (figure 10a) than the upstream-cylinder-generated, that is, Mode T-I is asymmetric about the wake centreline ($y^* = 0$).

E_u (figure 11) displays one peak at $St_1 = 0.192$ above the centreline and another at $St_2 = 0.234$ below the centreline, connected to the downstream- and upstream-cylinder-generated vortices, respectively. The lower-frequency peak becomes more prevailing at $x^* = 10$ (figure 11c) and 20 (figure 11d), indicating the more rapid decay of the upstream-cylinder-generated vortices owing to interactions between the streets (Sumner *et al.* 2000; Zhou *et al.* 2002). When P^* approaches 2.5 and α is close to 20°, both vortex frequencies are mostly discernible in E_u even at $x^* = 10 \sim 20$. In contrast, the higher vortex frequency disappears at $x^* = 5 \sim 7.5$ in Mode S-II (figure 9). In

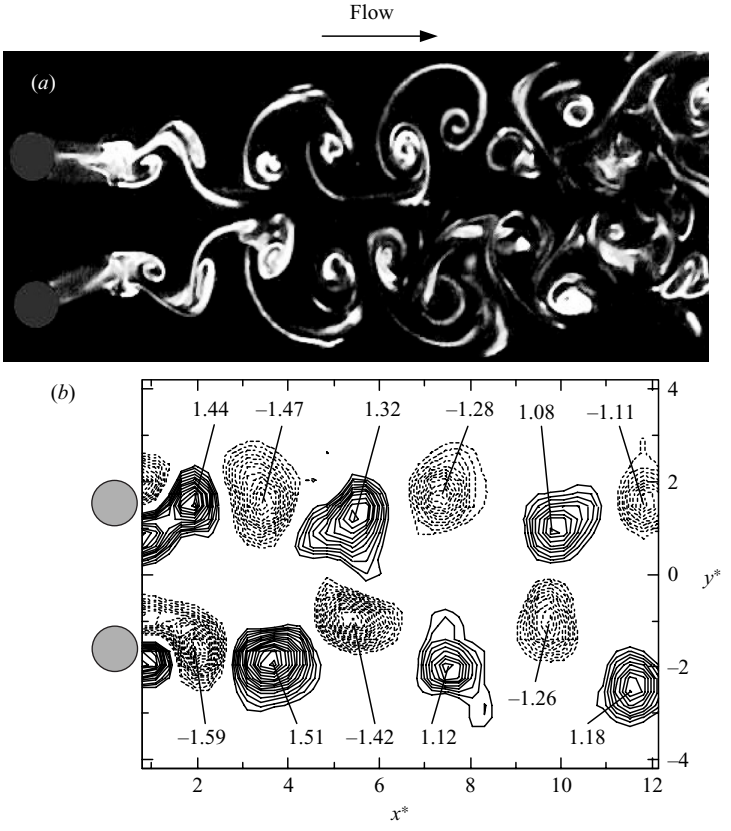

FIGURE 12. Typical instantaneous flow structure of Mode T-II ($P^* = 3.0$, $\alpha = 90°$). (*a*) Flow visualization ($Re = 300$); (*b*) PIV-measured vorticity contours ($Re = 7000$), the cutoff level = ± 0.3, the contour increment = ± 0.1.

general, a larger P or α corresponds to a longer survival for the upstream-cylinder-generated vortices of the higher frequency.

It is pertinent to mention that the two vortex frequencies deviate from each other by no more than 1%, which is comparable to experimental uncertainty in St (§ 3), for $P^* \geqslant 2.5$ and $\alpha = 88° \sim 90°$. However, the difference exceeds 2% at $\alpha = 86°$ or 84° and grows further for smaller P^* or α. Therefore, $\alpha = 88°$ is deemed to be a maximum incidence angle for Mode T-I.

4.4. *Mode T-II*

The flow structure of Mode T-II is essentially the same as the regime of two coupled vortex streets behind two side-by-side cylinders at $P^* \geqslant 2.5$ (e.g. Zdravkovich 1985). This regime was reported to occur at $P^* \geqslant 2.2$ behind two side-by-side cylinders (Sumner *et al.* 1999). The discrepancy between the present estimation and that in the literature is due to the uncertainty (± 0.25; see § 2) in estimating the critical P^*. Figure 12 presents one typical flow structure of this mode, where the two streets are anti-phased, or symmetrically arranged about $y^* = 0$, in contrast with Mode T-I (figure 10). The in-phase streets were also intermittently observed, though less stable (not shown). The two streets are characterized by approximately the same vortex strength and size (figure 12*b*). E_u is similar to that behind an isolated cylinder, with one pronounced peak at $St = 0.21$ across the wake for $x^* = 2.5 \sim 10$ (figure 13). This St

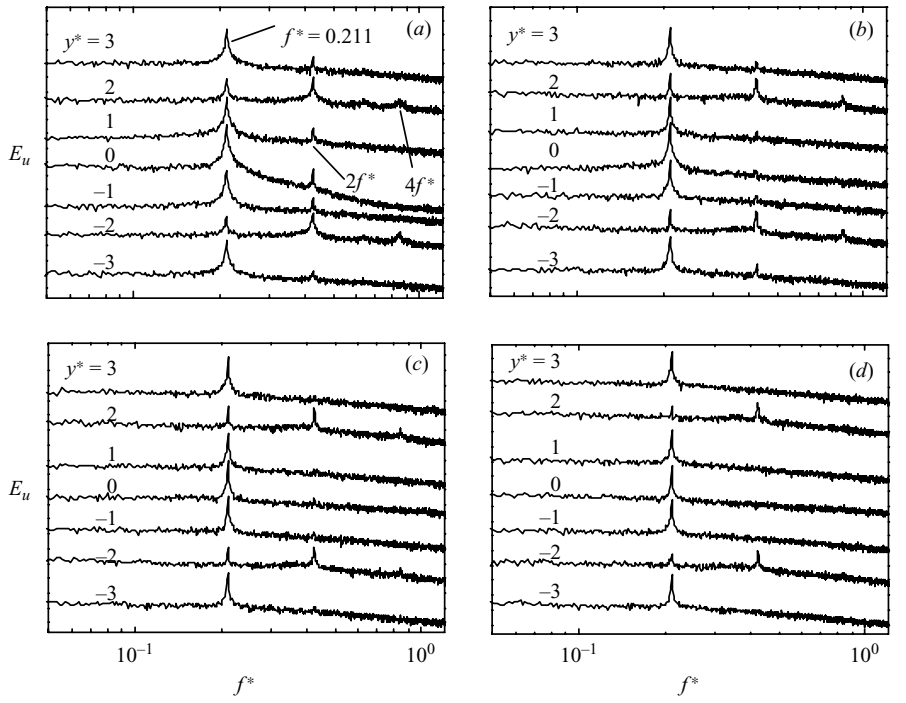

FIGURE 13. Power spectral density function, E_u, of the hot-wire signal u measured at (*a*) $x^* = 2.5$, (*b*) 5, (*c*) 7.5, (*d*) 10. $P^* = 3.0$ and $\alpha = 90°$ (Mode T-II). $Re = 7000$.

is unchanged, irrespective of P^* ($\geqslant 2.5$) or α ($\geqslant 88°$). The second and fourth harmonics of St are also discernible. The two cylinders behave individually like an isolated one. The results agree well with the previous reports of a two-side-by-side-cylinder wake at large spacing (e.g. Williamson 1985; Zhou *et al.* 2002).

4.5. *Summarized dependence of flow modes on P^* and α*

Figure 14 summarizes the classification of the flow structure based on P^* and α, which may be used to predict the flow structure as well as the dominant vortex frequencies in the wake of two staggered circular cylinders. A similar diagram was provided in figure 18 of Sumner *et al.* (2000). It should be pointed out that Sumner *et al.*'s diagram applies for the flow at $x^* < 6$, whereas figure 14 is valid for $x^* > 6$. The present flow structure modes and those identified by Sumner *et al.* are connected, and their correspondence is given in table 2. The present classification is consistent with the previous one at $\alpha = 0°$ or 90°. It is well known that the flow may be classified into three regimes at $\alpha = 0°$, i.e. the single-body regime, the reattachment regime and the co-shedding regime (Igarashi 1981; Zdravkovich 1987). For all three regimes, the flow behind the cylinders is characterized by a single vortex street (e.g. Zhou & Yiu 2006). While the single-body regime coincides with Mode S-Ia at $\alpha = 0°$, the other two regimes, characterized by a street of relatively weak vortices compared with that in the single-body regime (e.g. Zhou & Yiu 2006), correspond to Mode S-Ib. At $\alpha = 90°$, the flow is also divided into three regimes, i.e. the single vortex street regime, the asymmetrical wake regime and the coupled vortex street regime (e.g. Bearman & Wadcock 1973; Zdravkovich 1985; Zhou *et al.* 2002), which correspond well to Modes S-Ia, S-II and T-II, respectively.

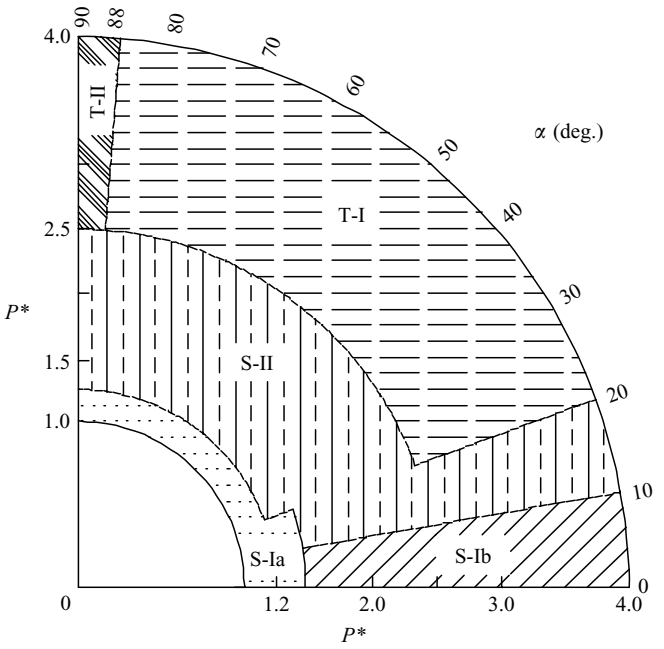

FIGURE 14. Dependence of flow structure on P^* and α in the wake of two staggered circular cylinders ($Re = 7000$).

It should be mentioned that the border, denoted by broken lines in figure 14, between different flow modes depends on Re as well as P^* and α, as demonstrated by Xu *et al.* (2003) in a two-side-by-side cylinder wake. The effect of Reynolds number is not examined at present. Owing to a limited number of configurations examined, the border is subjected to the uncertainties of $0.15 \sim 0.5$ in P^* and $\pm 5^\circ$ in α (§2). The change from one mode to another is in general characterized by a progressive transition, and a larger P^* corresponds to a smaller α at the occurrence of transition, or vice versa. A sudden change in the flow structure occurs only from Mode S-I to Mode S-II, as is evident from the densely populated iso-contours of St in figure 3(a). At $P^* > 1.5$ and $\alpha \approx 10^\circ$, the oncoming flow is suddenly deflected into the interstitial gap between the cylinders and the upstream cylinder begins generating high-frequency vortices, signalling a change from Mode S-Ib to Mode S-II. This change corresponds to the abrupt transition from *shear-layer reattachment* to *induced separation* flow pattern of Sumner *et al.* (2000). Mode S-Ia may directly transit to Mode S-II at $\alpha > 20^\circ$ when gap bleeding disappears and flow separation from the upstream cylinder occurs at a higher frequency for $P^* = 1.2 \sim 1.5$. This change corresponds to Sumner *et al.*'s (2000) abrupt transition from flow pattern of *base-bleeding* to *induced separation*. The transition from Mode S-Ia to Mode S-Ib takes place at $\alpha \leqslant 10^\circ$ and $P^* = 1.5 \sim 2.0$ when shear layers separating from the upstream cylinder reattach on the downstream. Mode S-II changes to T-I gradually at $P^* = 2.0 \sim 3.0$ and $\alpha = 20^\circ \sim 88^\circ$. With increasing P^* or α, interference between the two streets is less vigorous, resulting in the persistence of the two streets of different frequencies at $x^* = 10$ and beyond. Meanwhile, the ratio of the higher frequency to the lower diminishes, and the difference between the wake widths or vortex strengths of the two streets shrinks. This change corresponds to Sumner *et al.*'s (2000) transition of *vortex pairing and enveloping* or *vortex pairing, splitting and*

enveloping to *synchronized vortex shedding* flow pattern. The transition from Mode S-II to Mode T-II occurs at $P^* = 2.0 \sim 2.5$ and $\alpha \approx 90°$, and that from Mode T-I to Mode T-II takes place at $P^* \geqslant 2.5$ and $88° < \alpha < 90°$.

5. Discussion: flow structures and initial conditions

The four distinct modes of flow structure suggest distinct initial interactions among shear layers around the two cylinders. In order to explore the connection between flow structures and initial conditions, laser-induced fluorescence flow visualization was conducted at $Re = 7000$ in the wind tunnel under the same experimental conditions as PIV measurements. Smoke, generated from paraffin oil particles of 1 μm in diameter, was released from two pinholes of 0.75 mm in diameter, which were symmetrically drilled at about 60°, clockwise and anticlockwise, respectively, from the nominal leading stagnation point in the mid-span of each cylinder. The images were captured using the same CCD camera as PIV measurements. About 500 images were captured for each typical flow structure.

5.1. *Mode S-I*

5.1.1. *Mode S-Ia*

When two staggered cylinders are in close proximity ($P^* \leqslant 1.2$) or the downstream cylinder is completely submerged in the base region of the upstream cylinder, shear layers separated from the outer sides of the cylinders roll up to form one alternate vortex street (figure 15*a*, *b*), which appears similar to that behind an isolated cylinder. This flow structure may result from five distinct interactions of shear layers around the cylinders (figure 15*c*–*g*) based on the data in the literature as well as present measurements. The three flow patterns in figures 15(*c*) to 15(*e*) were reported by Sumner *et al.* (2000). As the two cylinders are in contact (figure 15*c*, *d*), the flow structure is essentially dependent on the rollup of two shear layers, resembling that behind an isolated cylinder. When the two cylinders are placed slightly apart ($P^* \leqslant 1.2$), the gap bleeding might penetrate into the base region of the upstream cylinder (figure 15*c*; also see figure 4*a*). The base bleeding plays a role in prolonging the vortex formation region (Sumner *et al.* 1999; Wang & Zhou 2005). Nevertheless, its influence is weak and the outer shear layers largely dictate the formation of the flow structure. At a higher *Re*, the inner shear layer separating from the upstream cylinder bifurcates (figures 15*a* and 15*f*). The same observation was made by Gu & Sun (1999) at $Re = 5600$ and Alam & Sakamoto (2005) at $Re = 55\,000$. While the outer shear layer, separating from the upstream cylinder, rolls up to form one row of vortices, the inner bifurcates once reattaching on the downstream cylinder, partly forming the gap flow between the cylinders and partly joining the shear layer separating from the downstream cylinder to form another row of vortices. In all four cases (figure 15*c*–*f*), the outer shear layers overwhelm the inner shear layers and dominate the formation of vortices, producing a vortex street both qualitatively and quantitatively similar to a single bluff-body wake. As the cylinders are placed slightly further apart ($P^* \leqslant 1.5$) and at $\alpha \leqslant 20°$, one shear layer separating from the upstream cylinder reattaches on the downstream cylinder before the formation of vortices, and the reattachment may or may not occur for the other shear layer (figure 15*g*), depending on α and *Re*. The downstream cylinder is essentially immersed in the base region of the upstream cylinder. Fluid between the two cylinders is relatively stagnant and the downstream cylinder, which may experience a thrust force (Igarashi 1981), acts to extend the upstream cylinder. One vortex street occurs behind the

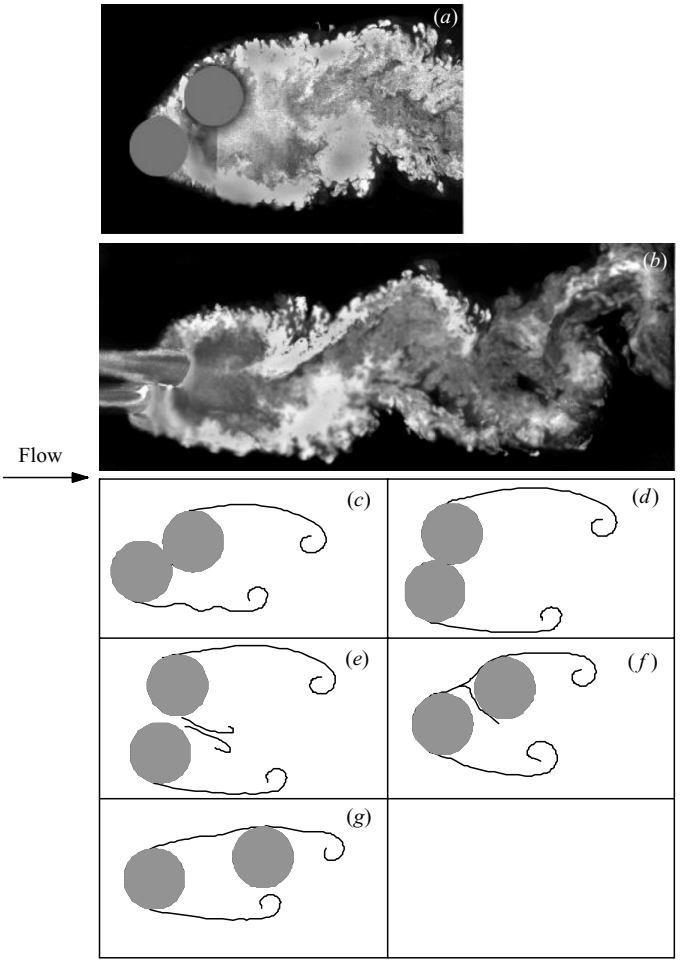

FIGURE 15. Photographs of Mode S-Ia from LIF flow visualization at $P^* = 1.2$ and $\alpha = 30^\circ$ ($Re = 7000$): (*a*) zoom-in shot, (*b*) zoom-out shot. (*c*)–(*g*) Schematic sketches of possible shear-layer interactions observed during flow visualization.

cylinders. Zhou & Yiu's (2006) phase-averaged data at $P^* = 1.3$, $\alpha = 0^\circ$ indicated that the maximum vorticity concentration associated with coherent structures was approximately the same as that behind an isolated cylinder. Although the five types of shear-layer interactions in figure 15(*c*–*g*) may differ qualitatively from each other, and may correspond to a rather large difference in C_L and C_d on both cylinders (please refer to the flow regime of *closely spaced staggered cylinders* in Sumner *et al.* 2005), the common feature is that the two cylinders behave like one single bluff body, generating one Kármán-type vortex street, i.e. Mode S-Ia.

5.1.2. *Mode S-Ib*

As P^* exceeds 1.5, three types of shear-layer interactions are possible at $\alpha \leqslant 10^\circ$. (i) Given $P^* = 1.8 \sim 4.0$, depending on Re, one shear layer separating from the upstream cylinder reattaches on and interacts with the shear layer around the downstream cylinder (figure 16*c*), and the other may interact vigorously with the shear layer separating from the downstream cylinder. One example is given in figure 6(*a*)

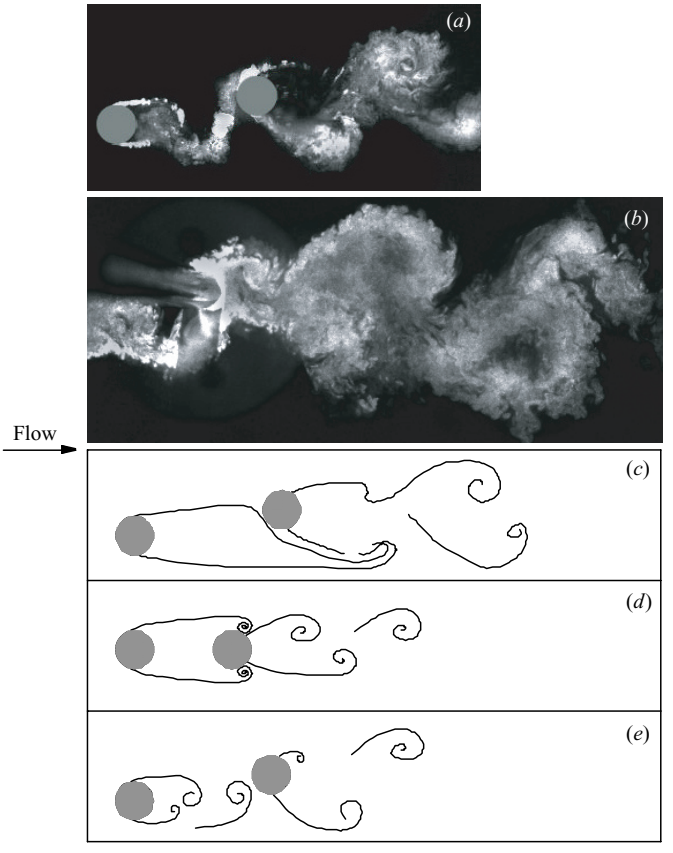

FIGURE 16. Photographs of Mode S-Ib from LIF flow visualization at $P^* = 4.0$ and $\alpha = 10^\circ$ ($Re = 7000$): (*a*) zoom-in shot, (*b*) zoom-out shot. (*c*)–(*e*) Schematic sketches of possible shear-layer interactions observed during flow visualization.

($P^* = 4.0$, $\alpha = 10^\circ$). (ii) For $P^* = 2.0 \sim 5.0$, depending on Re, and $\alpha \approx 0^\circ$, both shear layers separating from the upstream cylinder reattach on and interact with the shear layers around the downstream cylinder (figure 16*d*). See figure 4(*b*) ($Re = 500$, $P^* = 2.5$, $\alpha = 0^\circ$) in Xu & Zhou (2004) and figure 15 ($Re = 7000$, $P^* = 2.5$ and 4.0, $\alpha = 0^\circ$) in Zhou & Yiu (2006) for examples. (iii) At $P^* > 3.8 \sim 5.0$ and $\alpha \leqslant 10^\circ$, depending on Re, vortices are formed in the gap of the cylinders and impinge upon the downstream cylinder (figure 16*a*, *b*, *e*). In all the three cases, the shear layers or vortices from the upstream cylinder interact strongly with the shear layers around the downstream cylinder, resulting in postponed flow separation from the downstream cylinder and forming a street of greatly weakened vortices (Mode S-Ib) behind the downstream cylinder. Based on phase-averaged data at $P^* = 2.5$ and 6.0 and $\alpha = 0^\circ$ ($Re = 7000$, $x^* = 10 \sim 30$), Zhou & Yiu (2006) reported a maximum vorticity concentration of about 30% of that in an isolated cylinder wake (see their figure 7*j*).

Shear-layer reattachment may occur for Modes S-Ia and S-Ib (figure 15*f* and 16*c*). In Mode S-Ia, the two bluff bodies are closely separated ($P^* \leqslant 1.2$), and the inner shear layer separating from the upstream cylinder does not have sufficient space to develop before reattaching on the downstream cylinder. In fact, it may become part of the shear layer around the downstream cylinder, not having a significant impact on the vortex street behind the cylinders. In Mode S-Ib, however, the shear layers

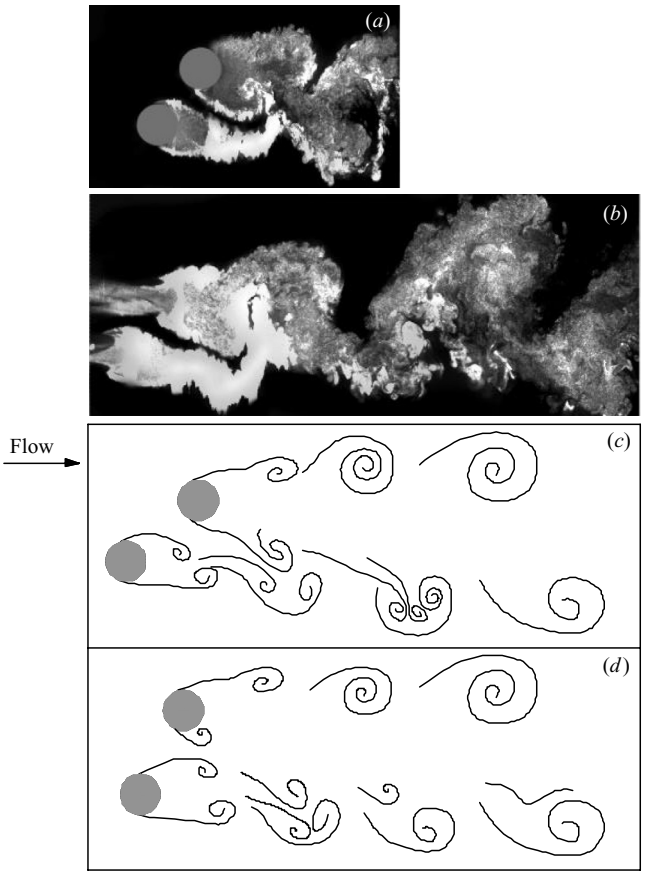

FIGURE 17. Photographs of Mode S-II from LIF flow visualization at $P^* = 2.0$ and $\alpha = 40^\circ$ ($Re = 7000$): (*a*) zoom-in shot, (*b*) zoom-out shot. (*c*)–(*d*) Schematic sketches of possible shear-layer interactions observed during flow visualization.

separating from the upstream cylinder have room to grow, and impinge upon the downstream cylinder, thus postponing flow separation from the downstream cylinder and producing a weakened vortex street.

5.2. *Mode S-II*

At a relatively large P^* and α ($1.2 < P^* < 2.5$ and $\alpha > 20^\circ$; $1.5 \leqslant P^* \leqslant 4.0$ and $10^\circ < \alpha \leqslant 20^\circ$), the two cylinders are separated so that the shear layers separating from the upstream cylinder will not reattach on the downstream cylinder, each cylinder producing a vortex street, with the vortex frequency behind the upstream cylinder exceeding twice that behind the downstream. Vigorous interactions between the two streets result in the survival of the lower-frequency street at $x^* = 5 \sim 7.5$ (figure 9). Two types of downstream evolution have been observed. (i) The two cross-stream vortices in the narrow street amalgamate with the inner vortex in the wide street, forming an asymmetrical wake at $x^* \geqslant 5$ (figure 17*a–c*). See figure 8(*a*) for example. (ii) The amalgamation of the three vortices is incomplete. Examples may be found in Sumner *et al.* (2000) at $P^* = 1.5$ and $\alpha = 60^\circ$ (see their figure 13*e*) and Wang & Zhou (2005) at $P^* = 1.7$ and $\alpha = 90^\circ$. The flow is characterized by gap vortex pairing, splitting and enveloping. Owing to incomplete amalgamation, three rows of vortices are present

in the combined near wake at $x^* \approx 6$, of which two rows of vortices are negatively signed and one row is positively signed (figure 17*d*). Further downstream, the negative vortices nearer to the flow centreline ($y^* = 0$) collapse (Wang & Zhou 2005), resulting in the occurrence of a single asymmetrical vortex street at $x^* \geqslant 10$. Wang & Zhou (2005) ascribed the occurrence of the two different downstream evolutions to a different phase relationship between the gap vortices. The amalgamation of the three vortices would occur (figure 17*c*) if the gap vortex in the wide street led in phase its counterpart in the narrow street, and would not (figure 17*d*) if the gap vortex in the wide street fell behind. In either case, the row of vortices resulting from the interaction of the narrow street and the inner row of vortices in the wide street is very weak, compared with that on the other side of the wake.

With increasing P^* or α, interactions between the two streets become less vigorous. Therefore, the narrow street survives longer, and it is more unlikely for the amalgamation of three vortices to occur. Sumner *et al.* (2000) referred to this as a transition from the flow pattern of *vortex pairing and enveloping* to *vortex pairing, splitting and enveloping*.

5.3. *Mode T-I*

At $P^* \geqslant 2.5$ and $20^\circ < \alpha < 88^\circ$, interactions among the four separated shear layers in mode T-I are less intensified, compared with those in Mode S-II, though still appreciable (figure 18; see also figure 10*a*). The street behind the upstream cylinder appears narrower and weaker in vortex strength (figure 10*b*) than that behind the downstream. The ratio of the higher frequency to the lower is approximately between 1.0 and 2.0, smaller than that of Mode S-II. The two streets of different frequencies persist even beyond $x^* = 10$ (figure 10). Sumner *et al.* (2000) referred to this flow structure as *synchronized vortex shedding* flow pattern in the near wake, whereas Akbari & Price (2005) called it *complete vortex shedding* flow regime.

5.4. *Mode T-II*

Mode T-II ($P^* \geqslant 2.5$ and $\alpha \geqslant 88^\circ$), the same as T-I, corresponds to Sumner *et al.*'s *synchronized vortex shedding* flow pattern in the near wake. However, interactions among the four separated shear layers in Mode T-II diminish further, though adequate to maintain the two streets coupled either anti-phased (figure 19*a–c*) or in-phase (figure 19*d*), with the same vortex frequency and strength as in an isolated cylinder wake.

6. Conclusions

Flow structures, dominant vortex frequencies and their downstream evolutions in the wake of two staggered circular cylinders were experimentally investigated using hot-wire, flow-visualization and PIV measurement techniques at $Re = 300$ and 7000. P^* was $1.2 \sim 4.0$ and α varied between 0° and 90°. Four distinct flow structures, along with their initial interactions of shear layers around the cylinders, are identified at $x^* = 10$, i.e. two single-street modes (S-I and S-II) and two twin-street modes (T-I and T-II), based on flow topology, vortex-shedding frequencies and their downstream evolutions.

Mode S-I is characterized by a single alternate vortex street, reasonably antisymmetric about the wake centreline. This mode is further divided into two different types, i.e. S-Ia and S-Ib, because of the considerable difference in their vortex strength. Mode S-Ia occurs when the two cylinders are in close proximity, i.e. at $P^* \leqslant 1.2$ ($\alpha = 0^\circ \sim 90^\circ$) or $P^* \leqslant 1.5$ ($\alpha \leqslant 20^\circ$). The pair of cylinders behaves like

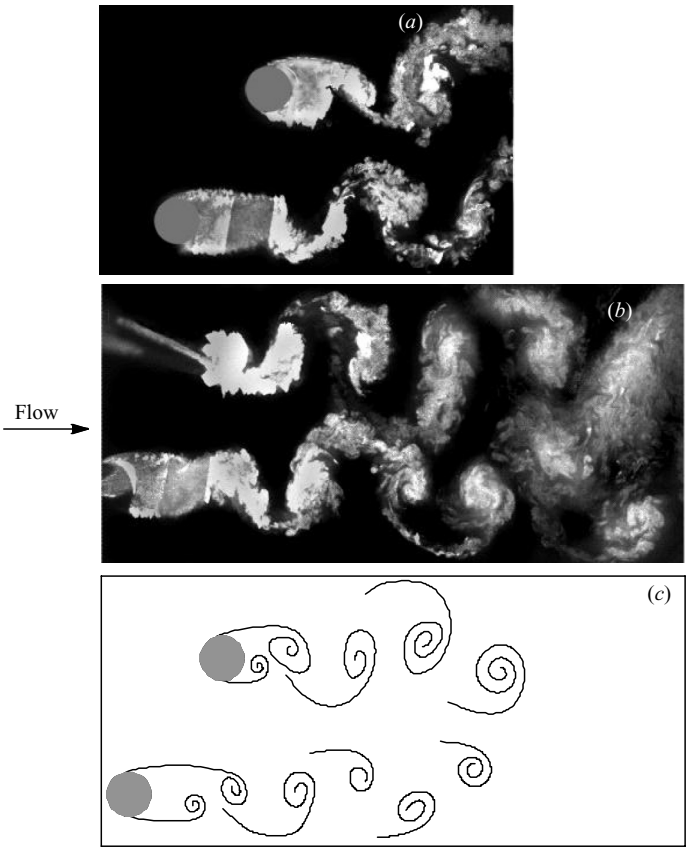

FIGURE 18. Photographs of Mode T-I from LIF flow visualization at $P^* = 4.0$ and $\alpha = 50^\circ$ ($Re = 7000$): (*a*) zoom-in shot, (*b*) zoom-out shot. (*c*) Schematic sketches of possible shear-layer interactions observed during flow visualization.

one body and shear layers separated from the free-stream sides of the cylinder pair roll up to form one alternate vortex street, which is qualitatively and quantitatively comparable to that behind an isolated cylinder. Mode S-Ib occurs at $P^* > 1.5$ and $\alpha \leqslant 10^\circ$. Shear layers separated from the upstream cylinder reattach onto or roll up to form vortices before reaching the downstream cylinder, resulting in the postponed flow separation from the downstream cylinder. Mode S-Ib is characterized by significantly weaker vortex strength (about 50% lower) and smaller vortex size, compared with Mode S-Ia. For both S-Ia and S-Ib, St is smaller than 0.21.

Mode S-II occurs at $1.2 < P^* < 2.5$ ($\alpha > 20^\circ$) or $1.5 \leqslant P^* \leqslant 4.0$ ($10^\circ < \alpha \leqslant 20^\circ$). Both cylinders generate vortices initially, forming one narrow street of higher St (>0.21) behind the upstream cylinder and one wide street of lower St (<0.21) behind the downstream at $x^* \leqslant 5.0$. The ratio of the higher frequency to the lower exceeds 2.0. The two streets interact vigorously, and the two upstream-cylinder-generated vortices of opposite signs amalgamate with the gap vortex generated by the downstream cylinder at $x^* = 5.0 \sim 7.5$, resulting in one single street of vortices at the lower St beyond $x^* = 10$. This street is asymmetric about the wake centreline, with the strength of vortices in the row on the upstream cylinder side about 50% lower than that in the other row.

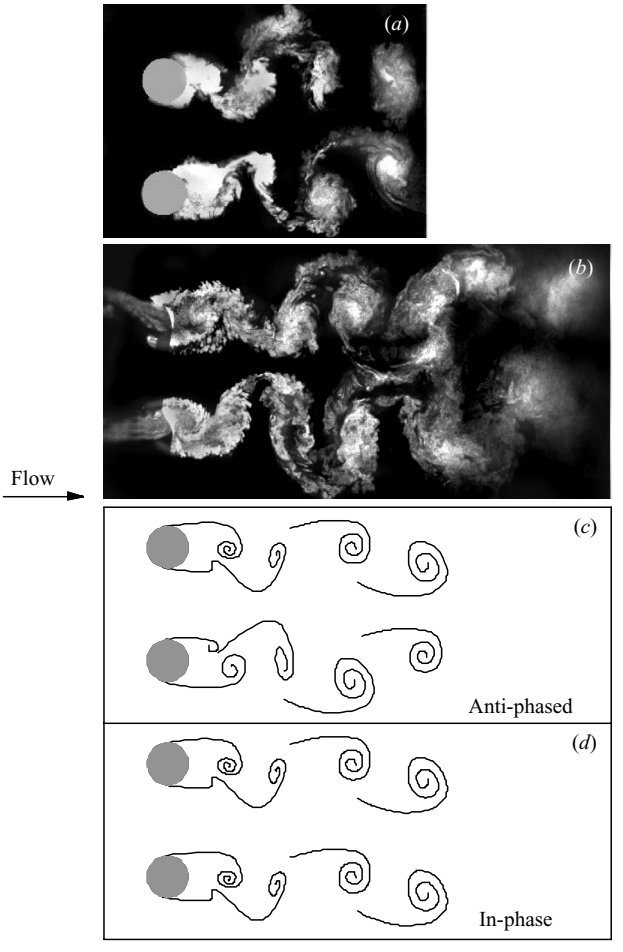

FIGURE 19. Photographs of Mode T-II from LIF flow visualization at $P^* = 3.0$ and $\alpha = 90°$ ($Re = 7000$): (*a*) zoom-in shot, (*b*) zoom-out shot. (*c*)–(*d*) Schematic sketches of possible shear-layer interactions observed during flow visualization.

Mode T-I occurs at $P^* \geqslant 2.5$ and $20° < \alpha < 88°$, where the two cylinders generate two distinct streets of different vortex strengths, widths and frequencies. Interacting less vigorously than in Mode S-II, both streets persist even beyond $x^* = 10$. Mode T-I is asymmetric about $y^* = 0$; the downstream-cylinder-generated vortices of the lower St (<0.21) are stronger, surviving longer than the upstream-cylinder-generated vortices of the higher St (>0.21). The ratio of the higher St to the lower varies between 1.0 and 2.0.

Mode T-II occurs at $P^* \geqslant 2.5$ and the line through the axes of cylinders is approximately normal to the incident flow ($\alpha \geqslant 88°$). The two streets, generated by each cylinder, of the same vortex frequency are coupled, mostly anti-phased or symmetric about $y^* = 0$. St is insensitive to a variation in P^* or α and is approximately 0.21, the same as that behind an isolated cylinder.

The dependence of the four flow modes on P^* and α is determined based on experimental data, which may be used to predict the flow structure as well as the dominant vortex frequencies in the wake of two staggered circular cylinders. Transition between the four modes with varying P^* and α is mostly progressive. Abrupt change

in the flow structure occurs only in the regions of $P^* = 1.2 \sim 1.5$ ($\alpha = 20^\circ \sim 90^\circ$) and $P^* > 1.5$ ($\alpha = 10^\circ \sim 20^\circ$), where Mode S-I changes to S-II.

Y. Z. wishes to acknowledge support given to him by the Research Grants Council of the Government of the HKSAR through Grant PolyU 5280/04E.

REFERENCES

Akbari, M. H. & Price, S. J. 2005 *J. Fluids Struct.* **20**, 533–554.

Alam, M. M. & Sakamoto, H. 2005 *J. Fluids Struct.* **20**, 425–449.

Bearman, P. W. & Wadcock, A. J. 1973 *J. Fluid Mech.* **61**, 499–511.

Gu, Z. F. & Sun, T. F. 1999 *J. Wind Engng Indust. Aerodyn.* **80**, 287–309.

Gu, Z. F., Sun, T. F., He, D. X. & Zhang, L. L. 1993 *J. Wind Engng Indust. Aerodyn.* **49**, 379–388.

Hu, J. C., Zhou, Y. & Dalton, C. 2006 *Exps. Fluids* **40**, 116–118.

Huang, J. F., Zhou, Y. & Zhou T. M. 2006 *Exps. Fluids* **40**, 884–896.

Ishigai, S., Nishikawa, E., Nishimura, E. & Cho, K. 1972 *Bull. JSME* **15**, 949–956.

Ishigai, S., Nishikawa, E. & Yagi, E. 1973 *In Pro. Symp. on Marine Engineering, Tokyo, Japan*, pp. 1-5-2–1-5-33.

Igarashi, T. 1981 *Bull. JSME* **24**, 323–331.

Igarashi, T. 1984 *Bull. JSME* **27**, 2380–2387.

Kim, H. J. & Durbin, P. A. 1988 *J. Fluid Mech.* **196**, 431–448.

Kiya, M., Arie, M., Tamura, H. & Mori, H. 1980 *Trans. ASME I: J. Fluids Engng* **102**, 166–173.

Kolár, V., Lyn, D. A. & Rodi, W. 1997 *J. Fluid Mech.* **346**, 201–237.

Mahir, N. & Rockwell, D. 1996 *J. Fluids Struct.* **10**, 473–489.

Price, S. J. 1976 *Aero. Q.* **27**, 154–168.

Price, S. J. & Païdoussis, M. P. 1984 *J. Wind Engng Indust. Aerodyn.* **17**, 329–347.

Raffel, M., Willert, C. E. & Kompenhans, J. 1998 *Particle Image Velocity: A Practical Guide.* Springer.

Sumner, D. & Richards, M. D. 2003 *J. Fluids Struct.* **17**, 345–350.

Sumner, D., Price, S. J. & Païdoussis, M. P. 2000 *J. Fluid Mech.* **411**, 263–303.

Sumner, D., Wong, S. S. T., Price, S. J. & Païdoussis, M. P. 1999 *J. Fluids Struct.* **13**, 309–338.

Sumner, D., Richard, M. D. & Akosile, O. O. 2005 *J. Fluids Struct.* **20**, 255–276.

Sun, T. F., Gu, Z. F., He, D. X. & Zhang, L. L. 1992 *J. Wind Engng Indust. Aerodyn.* **41**, 577–588.

Suzuki, N., Sato, H., Iuchi, M. & Yamamoto, S. 1971 In *Wind Effects on Buildings and Structures, Intl Wind Conf.*, Tokyo, Part II, pp. 20-1–20-10.

Wang, H. F., Zhou, Y., Chan, C. K. & Lam, K. S. 2006 *Phys. Fluids* **18**, 065106.

Wang, Z. J. & Zhou, Y. 2005 *Intl J. Heat Fluid Flow.* **26**, 362–377.

Williamson, C. H. K. 1985 *J. Fluid Mech.* **159**, 1–18.

Xu, G. & Zhou, Y. 2004 *Exps. Fluids* **37**, 248–256.

Xu, S. J., Zhou, Y. & So, R. M. C. 2003 *Phys. Fluids* **15**, 1214–1219.

Zdravkovich, M. M. 1977 *Trans. ASME I: J. Fluids Engng* **199**, 618–633.

Zdravkovich, M. M. 1985 *J. Sound Vib.* **101**, 511–521.

Zdravkovich, M. M. 1987 *J. Fluids Struct.* **1**, 239–261.

Zdravkovich, M. M. & Pridden, D. L. 1977 *J. Indust. Aerodyn.* **2**, 255–270.

Zhang, H. J. & Zhou, Y. 2001 *Phys. Fluids* **13**, 3675–3686.

Zhou, Y. & Yiu, M. W. 2006 *J. Fluid Mech.* **548**, 17–48.

Zhou, Y., Wang, Z. J., So, R. M. C., Xu, S. J. & Jin, W. 2001 *J. Fluid Mech.* **443**, 197–229.

Zhou, Y., Zhang, H. J. & Yiu, M. W. 2002 *J. Fluid Mech.* **458**, 303–332.